Analysis, Simulation, and Experiments of Dynamics and Control of a Hydrostatic Wind Turbine

A Thesis
SUBMITTED TO THE FACULTY OF THE
UNIVERSITY OF MINNESOTA
BY

Mark Andrew Leinberger

IN PARTIAL FULFILLMENT OF THE REQUIREMENTS
FOR THE DEGREE OF
MASTER OF SCIENCE

Professor Kim A. Stelson

2023

© Mark Andrew Leinberger 2023
ALL RIGHTS RESERVED

Acknowledgments

First and foremost, I would like to thank God for the strength and guidance He has given me up to this point. It is through His love and grace that I got to where I am now.

I am grateful for my advisor, Professor Kim Stelson. Our countless discussions have taught me to be curious. Professor Stelson has an unparalleled enthusiasm for research and inspires me to be a life-long learner.

I would also like to thank the other professors on my final exam committee, Professor Jim Van de Ven and Professor Kirsten Strandjord, for their valuable feedback and interest in my work.

I am also grateful for my colleague and friend, Dr. Daniel Escobar-Naranjo. Daniel has always been a voice of encouragement as I grew as a researcher and as a person. He taught me that I can also learn, as I teach.

I would also like to thank Dr. Biswaranjan Mohanty for his trusted counsel in my academic endeavors. Biswa is incredibly committed to advancing research in our group and has been instrumental in the success of my experimental design.

I would be remiss if I did not thank the other members of the fluid power transmission lab: Neil, Justin, Eric, and Mike. They all supported my work and motivated me to continue on.

I’d also like to recognize all of those people close to me who filled my life outside of school with so much light and joy. They have continued to remind me that I am a person first, and a student second. And for that, I am extremely grateful.

Finally, I would like to sincerely thank my family. My parents, Bill and Mary Leinberger, and my siblings, John and Annie, have always encouraged me to be myself and do what I love. I don’t know where I would be without their love and support and am eternally grateful to have these people I can call my home.

Dedication

I dedicate this work to my family.

Abstract

$K\omega^2$ control, also called torque control, is a popular tool for maximizing wind turbine power in region 2. For hydrostatic wind turbines, the $K\omega^2$ law relates pressure and rotor speed because pressure is proportional to torque. The $K\omega^2$ control law becomes pressure control with $p_c=K'\omega^2$. A new control law, Inverse $K\omega^2$ control, is proposed for rotor speed control with $\omega_c=(p/K')^{1/2}$. Both pressure- and rotor speed-regulation methods are investigated using P-, PI- and PID-control. This work analyzes the nonlinear dynamic interaction between HST wind turbines and the two $K\omega^2$ control methods.

Dimensionless, linearized models of these two approaches are used to investigate dynamics and control. Analysis shows that the mechanical rotor dynamics are much slower than the hydraulic transmission dynamics and that frictional and leakage losses have a negligible effect on system dynamics. Root locus analysis shows how systems responses change with variation of PID controller gains. Both control approaches require derivative controller action to sufficiently dampen their responses; both are also fundamentally limited in their speed of response by a slow stable pole regardless of their controller loop gains.

Nonlinear system simulation shows that both control approaches track the maximum power point with nearly identical transient behavior and have nearly identical power losses when using suboptimal values of the control law gain K. Experiments using the power regenerative hydrostatic test stand at the University of Minnesota – Twin Cities show that the control approaches have different transient responses but capture comparable power within 2% under steady, turbulent and nonideal conditions.

Table of Contents

Acknowledgments .... **i**
Dedication .... **iii**
Abstract .... **iv**
Table of Contents .... **v**
List of Tables .... **vii**
List of Figures .... **viii**
List of Notations .... **x**
1 Chapter 1: Introduction & Motivation **1**
- 1.1 Drive for Renewable Energy and Potential from Distributed Wind 1
- 1.2 Challenges in Distributed Wind with Hydrostatic Wind Turbines 2
- 1.3 Conventional Wind Turbine Control 5
- 1.4 Research Objectives 9
  - 1.4.1 Key Contributions 9
- 1.5 Chapter Overview 9

2 Chapter 2: Analysis of P-Controlled Linear Systems **10**
- 2.1 Modeling the Dynamic System 10
  - 2.1.1 Rotor Dynamics 10
  - 2.1.2 Pressure Dynamics 11
  - 2.1.3 Actuator Dynamics 11
  - 2.1.4 Generator Dynamics 11
- 2.2 Nondimensionalizing the Dynamic System 12
  - 2.2.1 Nondimensionalizing the Nonlinear Model 12
  - 2.2.2 $K\omega 2$ Law with Classical P-Control 14
  - 2.2.3 Dimensionless and Dimensioned Control Gains 15
- 2.3 Dynamic System Simplification – Neglecting Losses 15
- 2.4 Linearized Dynamics of $K\omega 2$-controlled Hydrostatic Wind Turbines 17
- 2.5 Steady-State Control Law Error 19
- 2.6 Root Locus Analysis of Linearized P-Control Dynamics 20
- 2.7 Conclusions about P-Controlled Systems 22

3 Chapter 3: Analysis of PI-Controlled Linear Systems **23**
- 3.1 $K\omega 2$ Law with Classical PI-control 23
- 3.2 Linearized Dynamics of $K\omega 2$-controlled Hydrostatic Wind Turbines 24

3.3 Steady-State Control Law Error 26
3.4 Root Locus Analysis of Linearized PI-Control Dynamics 27
3.5 Conclusions about PI-Controlled Systems 29
4 Chapter 4: Analysis of PID-Controlled Linear Systems 30
4.1 $K\omega2$ Law with Classical PID-control 30
4.2 Linearized Dynamics of $K\omega2$-controlled Hydrostatic Wind Turbines 31
4.3 Steady-State Control Law Error 34
4.4 Root Locus Analysis of Linearized PID-control Dynamics 34
4.5 Conclusions about PID-controlled Systems 38
5 Chapter 5: Numerical Simulations of Scaled Nonlinear Models 39
5.1 Simulation Results and Discussion 39
5.1.1 Ideal Conditions Study 39
5.1.2 Effect of Variation in a 44
5.1.3 Studying Effect of Variation in K at the Stationary Point 45
5.2 Conclusions from the Simulation Study 46
6 Chapter 6: Hardware-in-the-Loop Experiments on the Control of Hydrostatic Transmission Wind Turbines 47
6.1 Test Stand at the University of Minnesota – Twin Cities 47
6.2 Test Stand Control 49
6.2.1 Decoupling HSD and HST Control Loops 52
6.2.2 Designing Test Stand SISO Control Loops 53
6.3 Experiment Results and Discussion 56
6.3.1 Stepped Wind Study 56
6.3.2 Power capture study 59
6.3.3 Turbulent Wind Study 60
6.4 Conclusions from the Experimental Study 62
7 Chapter 7: Conclusions and Future Work 64
7.1 Conclusions 64
7.2 Future Work 65
7.2.1 Improvements to current study 65
7.2.2 Dynamically estimate rotor torque for MPPT control 66
7.2.3 Dynamically estimate wind speed and Model Predictive Control (MPC) 67
Bibliography 68
Appendices 72

List of Tables

Table 1. Specifications for a Polaris P21-60 60 kW Wind turbine 72

Table 2. Specifications for a 60kW Hydrostatic Wind turbine 73

Table 3. Scaling factors for various stationary points in region 2 73

Table 4. Typical values of c and ψ for a 60 kW HST wind turbine 75

Table 5. Typical parameter values for a 60 kW HST wind turbine 76

Table 6. Typical values of b and L for a 60 kW HST wind turbine 76

List of Figures

Figure 1. US electrical generation AEO2022 reference case 1

Figure 2. Conventional wind turbine drivetrain 2

Figure 3. HST wind turbine drivetrain 4

Figure 4. Regions of conventional wind turbine control, adapted from [8] 5

Figure 5. C_p vs. λ curve for 60 kW wind turbine (See Appendix 1 for turbine info) 6

Figure 6. Diagram of pressure-regulated hydrostatic wind turbine 14

Figure 7. Diagram of rotor speed-regulated hydrostatic wind turbine 14

Figure 8. LTI system in Evan's form [25] 20

Figure 9. Pole root loci for pressure-regulated system with P-control 21

Figure 10. Rotor speed zero root loci for pressure-regulated system with P-control 21

Figure 11. Pressure zero root loci for pressure-regulated system with P-control 21

Figure 12. Pole root loci for pressure-regulated system with PI-control 28

Figure 13. Rotor speed zero root loci for pressure-regulated system with PI-control 28

Figure 14. Pressure zero root loci for pressure-regulated system with PI-control 28

Figure 15. Pole root loci of pressure- regulated (left) and rotor speed-regulated (right) systems with PID-control for $ri = 5$ and $rd = 0.1$ 35

Figure 16. Rotor speed zero root loci for pressure-regulated system with PID-control for $ri = 5$, $rd = 0.1$ 36

Figure 17. Pressure zero root loci for pressure-regulated system with PID-control for $ri = 5, rd = 0.1$ 36

Figure 18. Closed-loop poles and zeros for $Kp,pr = 5$, $Kp,rs = 10$, $ri = 5$ and $rd = 0.1$ 37

Figure 19. Dimensionless state and power time responses of systems initialized at the stationary point. 40

Figure 20. Dimensionless state and power time responses of systems initialized arbitrarily away from the stationary point. 41

Figure 21. Phase portrait of rotor speed and pressure responses of systems initialized arbitrarily away from the stationary point. 42

Figure 22. Dimensionless state and power time responses of systems initialized away from the stationary point to reflect initial operation at 5 m/s wind.....43

Figure 23. Phase portrait of rotor speed and pressure responses of systems initialized away from the stationary point to reflect initial operation at 5 m/s wind.....44

Figure 24. Dimensionless power responses of systems with a = 1 (top), a=2 (middle) and a=4 (bottom)....45

Figure 25. Power capture with variation in K 46

Figure 26. HST test stand at the University of Minnesota – Twin Cities.....47

Figure 27. Test stand control setup 3.....51

Figure 28. Test stand control setup 2.....52

Figure 29. Frequency response of closed-loop HST pressure (left) and HST rotor speed (right) control.....54

Figure 30. HST pressure (left) control loop gain and rotor speed control loop gain (right).....55

Figure 31. Stepped wind profile.....56

Figure 32. Reference, output and error responses of pressure-regulated system under stepped wind.....57

Figure 33. Reference, output and error responses of rotor speed-regulated system under stepped wind.....57

Figure 34. Dimensionless state and power responses under stepped wind.....58

Figure 35. Power capture as a function of control law gain.....60

Figure 36. Dimensionless state and power responses under turbulent wind with mean wind speed v=6 m/s.....61

Figure 37. Scaled power curves and fitted power characteristics at v=3,6,9 m/s.....74

Figure 38. Pole root loci of pressure-regulated system with PI-control for chosen values of ri.....77

Figure 39. Rotor speed zero root loci of pressure-regulated system with PI-control for chosen values of $ri \leq 23$.....78

Figure 40. Pressure zero root loci of pressure-regulated system with PI-control for chosen values of ri.....79

Figure 41. Swashplate zero root loci of pressure-regulated system with PI-control for chosen values of ri 79

Figure 42. Root loci of pressure-regulated system with PID-control for chosen ri and rd.....81

List of Notations

α	normalized swashplate position
α_{cmd}	command normalized swashplate position
a	dimensionless power characteristic curvature
A	rotor swept area [m^2]
B	Blade pitch angle [rad]
β	effective bulk modulus [Pa]
c^2	ratio of rotor and hydraulic response times
C_p	rotor power coefficient
$C_{p.max}$	maximum power coefficient
D_p	hydraulic pump displacement [m^3/rev]
D_m	hydraulic motor max displacement [m^3/rev]
J	rotor inertia [kgm^2]
K	control law gain [Nms^2/rad^2]
λ	tip speed ratio (TSR)
λ_*	optimal TSR corresponding to $C_{p,max}$
ω	rotor angular speed (rad/s)
ω_h	generator angular speed [rad/s]
p	HST pressure [Pa]
P_r	Rotor Power [W]
P_w	Wind Power [W]
ρ	air density [kg/m^3]

R	rotor radius [m]
ψ	ratio of rotor and actuator response times
T	aerodynamic torque [Nm]
τ_{sp}	swashplate actuator time constant [s]
v	wind speed [m/s]
V	HST hose volume [m^3]
x_m	scaling factor
$\hat{x}$	dimensionless value

1 Chapter 1: Introduction & Motivation

Because of rising global carbon dioxide emissions and temperatures, advancements in renewable energy give hope for a cleaner and healthier future. Figure 1 shows how electricity production trends in the United States [1].

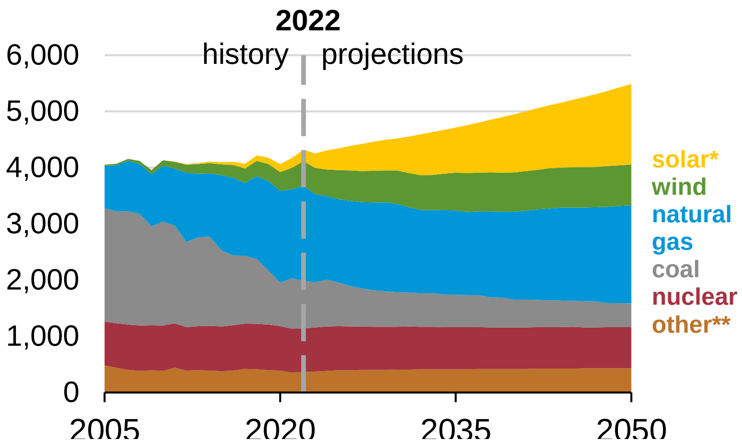

Figure 1. US electrical generation AEO2022 reference case

Wind energy is the fastest growing renewable energy source in the world [2]. Wind currently makes up 8% of the United States' electricity production [3]. The United States has a goal to reach 20% capacity by the year 2030 and 35% capacity by the year 2050 [4].

1.1 Drive for Renewable Energy and Potential from Distributed Wind

Utility-scale wind turbines rated above one MW dominate the wind energy market, with a recent emphasis on off-shore opportunities [3]. Larger wind turbines have larger blade-swept areas higher up from the earth's surface allowing higher power capture and reduced effects of topographical contours on the earth's surface. Locations best-suited for larger wind turbines often distance the utility-scale wind farms from the end users. This increases transmission costs.

Distributed wind energy shortens the distance between the wind turbines and the end users. Rather than using utility-scale wind turbine farms designed to support the larger grid, distributed wind needs can be satisfied by smaller-scale wind turbines. Mid-sized wind turbines rated between 100 kW and 1 MW offer an attractive option for community-scale end users such as farms, factories, and electric cooperatives. Taking advantage of mid-sized wind turbines in these areas can improve grid stability, reduce transmission costs and increase total clean energy production [5].

1.2 Challenges in Distributed Wind with Hydrostatic Wind Turbines

Distributed wind is challenged by higher Levelized Cost of Electricity (LCOE) in smaller wind turbines than larger wind turbines [6]. This motivates alternative measures to reduce mid-sized wind turbine costs. Conventional wind turbines use a fixed-displacement planetary gearbox and power converter to transfer power to the grid. Unsteady wind conditions subject the gearbox to shock loading which can damage it and reduce reliability. The power electronics also add a layer of technological complexity and significant hardware costs [7]. A conventional gearbox wind turbine is shown in Figure 2.

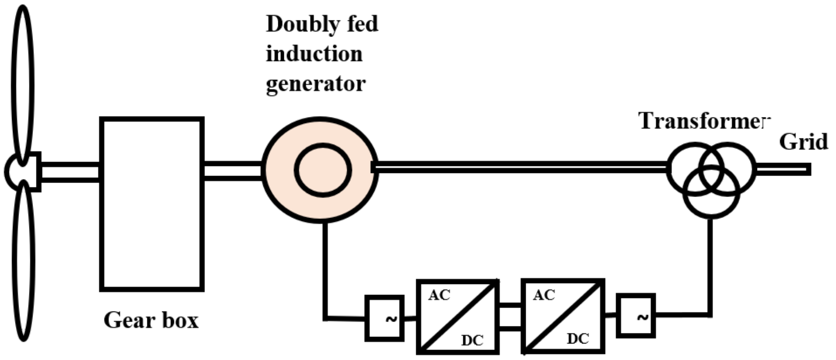

Figure 2. Conventional wind turbine drivetrain

Hydrostatic transmissions (HST) are an alternative to gearboxes in conventional wind turbines. An HST is a continuously-variable transmission (CVT) with high power density, reliability, and operating flexibility. High operating pressures involved in the power transfer allows for significantly higher power density with small hydraulic components. This means that smaller components can be used which reduces the overall wind turbine weight and cost. The power is transferred through a slightly compressible fluid which absorbs energy from shock loading under unsteady wind conditions, protecting the components and increasing the reliability. HSTs used in vehicles are speed-down transmissions while wind turbine drivetrains require a speed-up transmission to convert power from the low-speed rotor to the high-speed generator. A synchronous generator transfers power from the HST to the grid decoupling the rotor from the synchronous generator.

Retrofitting wind turbines with HSTs is not a new concept. Rather, it has an intensive research history around the world [8]. Chapdrive in Norway built an early 1 MW hydrostatic wind turbine and studied its ability to operating under various wind conditions and grid faults [9]. Artemis Intelligent Power developed digital displacement control to decouple the synchronous generator speed from the variable rotor speed and improve transmission efficiency. Artemis built a 1.5 MW hydrostatic tests stand to study their design [10]. Mitsubishi continued this work by teaming with Artemis engineers to build multiple 7 MW offshore hydrostatic wind turbines which consisted of a digital displacement pump and two digital displacement motors. Called SeaAngel, this project boasted the largest digital displacement transmission in existence at the time which operated off the coasts of Scotland and Japan [11]. RWTH Aachen built a 1 MW hydrostatic test stand to investigate the possibility of a more complex transmission in which the controller switched between multiple pumps to accommodate different operating conditions [12] The University of Minnesota built a 100 kW hydrostatic test stand to investigate the use of hydrostatic wind turbines in community scale wind applications. This smaller-scale single fixed-displacement pump and single variable-displacement motor architecture consists of components that are available off-the-shelf [13].

This work focuses on an HST that consists of a fixed-displacement pump driven by the rotor and a variable-displacement motor that drives the generator where the continuously-variable displacement ratio varies with the position of a swashplate in the variable-displacement motor. A schematic of an HST wind turbine drivetrain is shown in Figure 3.

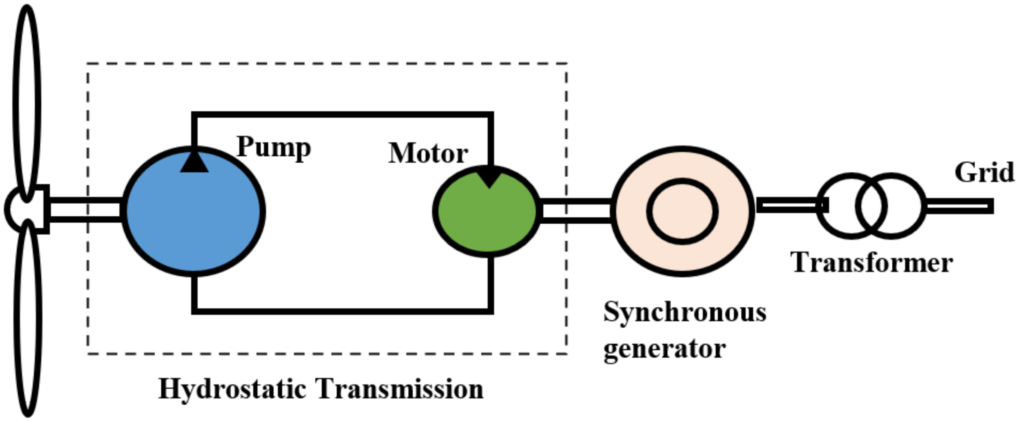

Figure 3. HST wind turbine drivetrain

While using an HST in a wind turbine has benefits, it inherently has both mechanical and volumetric losses which result in a slightly lower efficiency than that of a conventional gearbox transmission. However, improvements can be made by better understanding HST wind turbine dynamics and control.

1.3 Conventional Wind Turbine Control

Conventional wind turbine control has four regions of operation. A supervisory controller selects a different control strategy for each region. In region 1 the wind speed is too low to generate significant power. In region 2 the wind turbine is below rated power and is operated to maximize power. In region 3 the wind turbine is above rated power and is regulated to maintain rated power. In region 4 the wind speed is high enough to damage the wind turbine, so the wind turbine is braked. These four regions are shown in Figure 4.

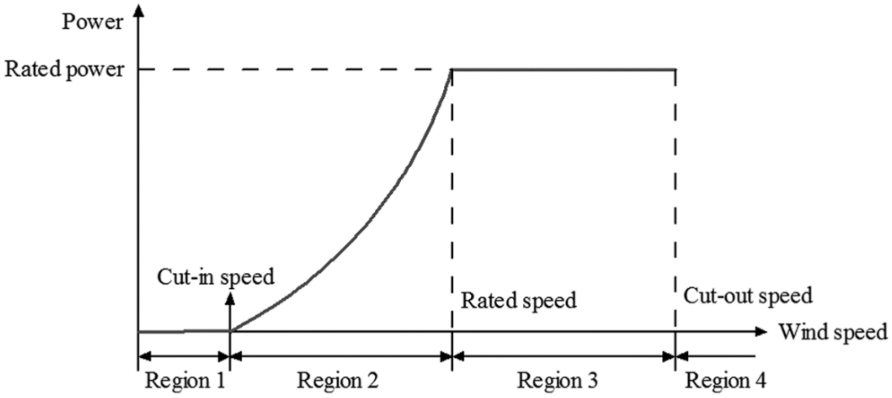

Figure 4. Regions of conventional wind turbine control, adapted from [8]

Unsteady wind conditions shift the wind turbine between regions 2 and 3, giving rise to situations in which the wind turbine goes from dissipating above-rated energy to capturing as much below-rated energy as possible. This poses an opportunity for improving power capture. A hydraulic accumulator coupled to the rotor shaft can store excess energy in region 3 and release that energy in region 2 [14].

This work focuses on understanding the dynamics and control of hydrostatic horizontal wind turbines in region 2. Power is maximized in region 2 by tracking the peak of the C_p vs. λ curve. The power coefficient C_p is the dimensionless ratio of power captured by the rotor to the power from the wind.

$$C_p = \frac{P_r}{P_w} = f(\lambda, \mathrm{B}) \tag{1.1}$$

The tip-speed ratio λ is the dimensionless ratio of tangential speed at the tip of the rotor blades to the wind speed.

$$\lambda = \frac{\omega R}{v} \tag{1.2}$$

The wind power is a function of the air density ρ, blade-swept area A, and wind speed v.

$$P_w = \frac{1}{2}\rho A v^3 \tag{1.3}$$

The rotor power is the product of the aerodynamic torque from the wind τ and rotor angular speed ω.

$$P_r = T\omega \tag{1.4}$$

C_p is also a function of the blade pitch angle B. Assuming zero blade pitch in region 2, C_p reduces to the two-dimensional plot in Figure 5.

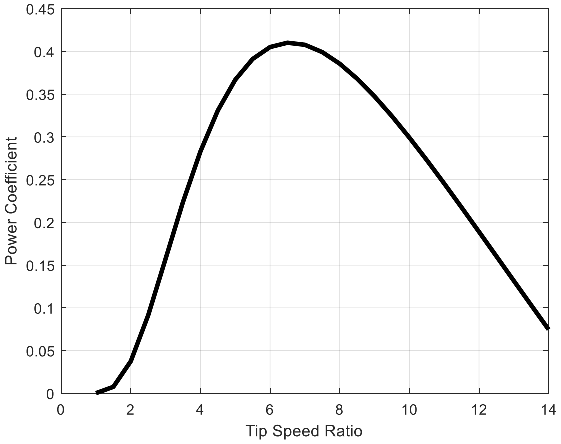

Figure 5. C_p vs. λ curve for 60 kW wind turbine (See Appendix 1 for turbine info)

C_p is approximately parabolic near the peak at $(\lambda_*, C_{p,max})$. The steady-state power transfer at the peak is given in Equation 1.5.

$$\frac{1}{2} C_{p,max} \rho A v^3 = T_{opt} \omega_{opt} \tag{1.5}$$

The relationship between rotor torque and rotor speed is derived from (1.5).

$$T_{opt} = K \omega_{opt}^2 \tag{1.6}$$

Conventional wind turbine region 2 control uses this $K\omega^2$ law to drive the generator torque as a function of rotor speed to its optimal value for maximum power capture. This is an example of Maximum Power Point Tracking (MPPT) control.

$$T_c = K \omega^2 \tag{1.7}$$

This is an attractive method because it does not require wind speed measurement [15]. Leithead et. al. suggested implementing $K\omega^2$ control using either rotor torque or rotor speed control [16][17]. This introduces a rotor speed-regulated system in which a rotor speed command ω_{ref} is tracked.

$$\omega_c = \sqrt{\frac{\hat{T}}{K}} \tag{1.8}$$

Where $\hat{T}$ is an estimate of the generator torque from a Kalman filter. Leithead claimed that the torque and speed control methods yielded the same steady performance but did not expand the study to unsteady or nonideal conditions.

In a hydrostatic wind turbine, the transmission pressure command, p_c , is given by:

$$p_c = \frac{2\pi}{D_p} K\omega^2 \tag{1.9}$$

Pressure-regulation is used in [13,14,18,19]. A method of rotor speed-regulation is used in [20] but requires wind speed measurement. The current study extends the idea of $K\omega^2$-based rotor speed-regulation to hydrostatic wind turbines where the rotor speed command, ω_c , is given by:

$$\omega_c = \sqrt{\frac{D_p p}{2\pi K}} \tag{1.10}$$

Both methods require an accurate value of K which depends on high powers of the parameters as shown in Equation 1.11.

$$K = \frac{\frac{1}{2}\,\rho\pi R^5\, C_{p,max}}{\lambda_*^3} \tag{1.11}$$

Effective rotor radius may vary with time and optimal TSR is difficult to estimate. Variations as small as 5% in λ_* can reduce annual power capture by 1-3% [21]. Johnson et. al., Escobar-Naranjo et. al., and others investigated model-free MPPT approaches in search of more robust options. Their results yielded higher power capture in uncertain conditions but slow convergence times [15],[19].

Better understanding hydrostatic wind turbine dynamics and $K\omega^2$ control will guide further work in other advanced control methods. Literature discussing how $K\omega^2$ control affects wind turbine dynamics includes a study at the National Renewable Energy Laboratory showing that a $K\omega^2$ torque-controlled gearbox hydrostatic wind turbine is stable in the sense of Lyapunov under certain conditions [19].

1.4 Research Objectives

The goal of this research is to investigate dynamics and control of two $K\omega^2$ control approaches for hydrostatic wind turbines: pressure-regulation and rotor speed-regulation.

1.4.1 Key Contributions

- Generalizing the analysis and simulation by nondimensionalizing the system model.
- Showing that energy losses from rotor damping and HST leakage are negligible.
- Showing how dynamics of $K\omega^2$ pressure- or rotor speed-controlled HST turbine vary for a wide range of tunable parameters.
- Validating analytical assertions using simulation and experiments.

1.5 Chapter Overview

This thesis is divided into 6 chapters. Linear analysis of P-controlled, PI-controlled and PID controlled systems is presented in chapters 2, 3 and 4. In chapter 5, nonlinear simulations are used to validate the linear analysis and expand the study to nonlinearities. In chapter 6, experiments on the power-regenerative HST test stand at the University of Minnesota are compared to the analysis and simulations. . Conclusions and future work are discussed in chapter 7.

2 Chapter 2: Analysis of P-Controlled Linear Systems

2.1 Modeling the Dynamic System

The HST transfers power from the low-speed rotor to the high-speed generator. Mohanty and Stelson [18] modeled this HST transmission using bond graphs resulting in dynamic equations for rotor angular speed ω, transmission line pressure p, swashplate actuator normalized position α and generator speed ω_h.

2.1.1 Rotor Dynamics

The rotor speed dynamics come from a torque balance on the rotor shaft:

$$J\dot{\omega}_r = T - \frac{D_p}{2\pi}p \tag{2.1}$$

where J is the rotary inertia of the rotor, T is the aerodynamic torque imposed on the rotor shaft from the wind, and D_p is the displacement of the hydraulic pump. This neglects losses due to damping which will be validated later. The aerodynamic torque T is related to the power P which, for constant wind, is locally parabolic near the maximum value at ω_m as shown in Equation 2.2.

$$P = P_m - \mathrm{A}(\omega - \omega_m)^2 \tag{2.2}$$

Where $\mathrm{A} \geq 0$ and the subscript m denotes the wind turbine operating point at the peak of this parabolic curve.

2.1.2 Pressure Dynamics

The dynamics of the transmission line pressure come from the flows in and out of a control volume in the transmission line. The flow in comes from the hydraulic pump and the flow out to the variable-displacement hydraulic motor:

$$\dot{p} = \frac{\beta D_p}{2\pi V}\omega - \frac{\beta D_m \omega_h}{2\pi V}\alpha \tag{2.3}$$

where β is the effective bulk modulus, V is the effective fluid volume, and D_m is the maximum displacement of the hydraulic motor. This neglects volumetric and mechanical losses which will be validated in the following analysis.

2.1.3 Actuator Dynamics

The dynamics of the actuator are identified from experiments using the HST test bed described in Chapter 5. The actuator is modeled as a first order system with command swash plate α_{cmd} as input and actual swashplate position α as output:

$$\dot{\alpha} = \frac{1}{\tau_{sp}}(\alpha_{cmd} - \alpha) \tag{2.4}$$

where τ_{sp} is the actuator time constant.

2.1.4 Generator Dynamics

The synchronous generator dynamics come from a torque balance on the generator shaft.

$$J_h \dot{\omega}_h = T_e + \frac{\alpha D_m}{2\pi} p \tag{2.5}$$

Where J_h is the rotational inertia of the generator. These dynamics are dominated by the electrical inertia of the grid, so the generator speed will be assumed to be constant [22].

2.2 Nondimensionalizing the Dynamic System

2.2.1 Nondimensionalizing the Nonlinear Model

Non-dimensional variables increase the conciseness and understandability of the state equations. The states and time are expressed as nondimensional variables using the following equations:

$$\widehat{\omega} = \frac{\omega}{\omega_m}, \qquad \hat{p} = \frac{p}{p_m}, \qquad \hat{\alpha} = \frac{\alpha}{\alpha_m}, \qquad \hat{t} = \frac{t}{t_m} \tag{2.6}$$

The scaling factors of the states are found by normalizing using the steady-state operating condition at the maximum power point. Using the steady state equations and the $K\omega^2$ law gives these scaling factors:

$$\omega_m = \sqrt{\frac{T_m}{K}} \tag{2.7}$$

$$p_m = \frac{2\pi T_m}{D_p} \tag{2.8}$$

$$\alpha_m = \frac{D_p}{D_m \omega_h} \sqrt{\frac{T_m}{K}} \tag{2.9}$$

The time scaling factor is the time required to accelerate the rotor from zero to ω_m:

$$t_m = \frac{J\omega_m}{T_m} \tag{2.10}$$

The dimensionless aerodynamic torque $\hat{T}$ is related to the dimensionless power $\hat{P}$ which has a parabolic characteristic local to point m where $\widehat{\omega} = 1$ as shown in equation (2.11). Based on the data from [16] presented in Appendix 1, a is assumed to be 2.

$$\hat{P} = 1 - a(\widehat{\omega} - 1)^2 \tag{2.11}$$

The power characteristic is divided by $\widehat{\omega}$ and substituted for $\hat{T}$. The dimensionless dynamics equations are shown in equations (2.11)-(2.13).

$$\dot{\widehat{\omega}} = \frac{1-a}{\widehat{\omega}} - a\widehat{\omega} + 2a - \hat{p} \tag{2.11}$$

$$\dot{\hat{p}} = c^2(\widehat{\omega} - \hat{\alpha}), \qquad c = \frac{D_p}{2\pi}\sqrt{\frac{\beta J}{V T_m K}} \tag{2.12}$$

$$\dot{\hat{\alpha}} = \psi(\hat{\alpha}_{cmd} - \hat{\alpha}), \psi = \frac{J\omega_m}{T_m \tau_{sp}} \tag{2.13}$$

This model generalizes the equations to any size hydrostatic wind turbine that has a fixed-displacement pump and variable-displacement motor. Data from a 60-kW wind turbine [22,23] shows that $c = 26$ and $\psi = 25$ for steady-state operation at 6 m/s. See Appendix 1 for information on a typical 60-kW wind turbine. It is expected that $c^2 \gg 1$ and $\psi \gg 1$ for a wide range of hydrostatic wind turbine sizes and operating conditions. This means that the hydrostatic transmission and swash plate response is much faster than the rotor response. The normalized dynamic equations also show that rotor damping and transmission leakage losses are negligible and can be neglected. It is expected that this would be true generally.

2.2.2 $K\omega^2$ Law with Classical P-Control

Classical controllers are used to command $\hat{\alpha}_{cmd}$ for MPPT. with either pressure- or rotor speed-regulation using the $K\omega^2$ law. P-control determines the command using equation 2.14.

$$\hat{\alpha}_{cmd} = \widehat{K}_p \hat{e} \tag{2.14}$$

where $\hat{e}$ is $\hat{e}_{pr} = \hat{p} - \widehat{\omega}^2$ for pressure and $\hat{e}_{rs} = \sqrt{\hat{p}} - \widehat{\omega}$ for rotor speed control. $\widehat{K} = 1$ so the control law error goes to zero at the peak of the dimensionless power characteristic. $\hat{e}$ creates nonlinear since the $K\omega^2$ law adds nonlinearity to the system dynamic models. The nonlinear pressure- and rotor speed-regulated hydrostatic wind turbines are shown as block diagrams in figures 6 and 7.

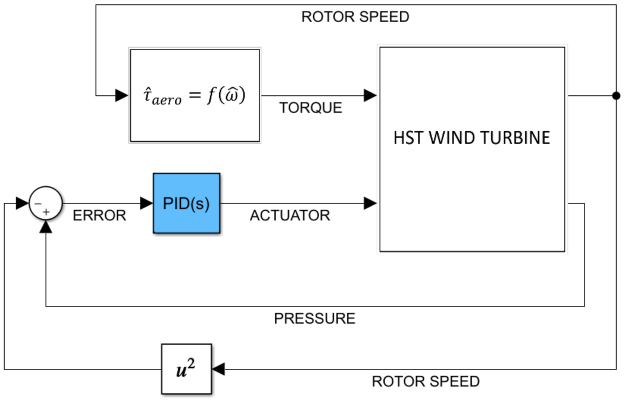

Figure 6. Diagram of pressure-regulated hydrostatic wind turbine

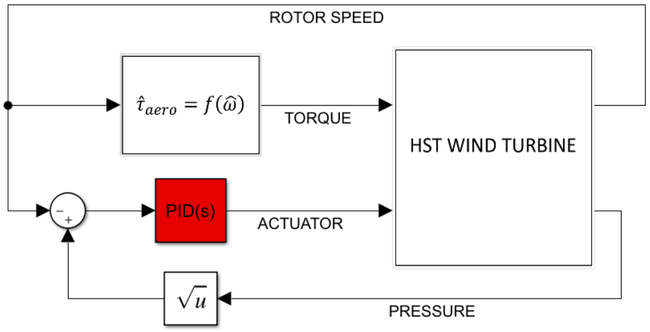

Figure 7. Diagram of rotor speed-regulated hydrostatic wind turbine

The two systems have identical plants but track different control law errors because of their differing control laws..

2.2.3 Dimensionless and Dimensioned Control Gains

The dimensionless control gain $\widehat{K}_p$ commands the dimensionless control input using dimensionless error, but the dimensional control gain K_p commands the normalized swashplate position using the error in Pascals for the pressure-regulated system or in rad/s for the rotor speed-regulated system to the unitless swashplate position. The conversion between the dimensionless and dimensioned control gains is given in Equation 2.15 for the pressure-regulated system and Equation 2.16 for the rotor speed-regulated system.

$$K_p = \frac{D_p^2}{2\pi D_m \omega_h} \sqrt{\frac{1}{T_m K}} \widehat{K}_p \tag{2.15}$$

$$K_p = \frac{D_p}{D_m \omega_h} \widehat{K}_p \tag{2.16}$$

The conversion for the pressure-regulated control gain depends on the operating conditions since it includes T_m .The conversion for the rotor speed-regulated control gain is independent of the operating condition. This conversion also applies to PI- and PID-controlled hydrostatic wind turbines in chapters 3 and 4.

2.3 Dynamic System Simplification – Neglecting Losses

The dimensionless dynamic equations derived in the previous section neglect rotor damping and leakage losses. The dimensionless rotor speed and pressure dynamic equations with loss terms included are given in Equations 2.17 and 2.18 where b-hat is the dimensionless damping coefficient and L-hat is the dimensionless leakage coefficient.

$$\frac{d\widehat{\omega}}{d\hat{t}} = \hat{T} - \hat{b}\widehat{\omega} - \hat{p} \tag{2.17}$$

$$\frac{d\hat{p}}{d\hat{t}} = c^2\left(\widehat{\omega} - \hat{\alpha} - \hat{L}\hat{p}\right) \tag{2.18}$$

The values of $\hat{b}$ and $\hat{L}$ are derived by nondimensionalizing the dynamic equations with losses included. The resulting dimensionless loss terms are given in Equations 2.19 and 2.20.

$$\hat{b} = b\sqrt{\frac{1}{T_m K}} \tag{2.19}$$

$$\hat{L} = \frac{4\pi^2\sqrt{T_m K}}{D_p^2} L \tag{2.20}$$

The conditions for b and L to be negligible are given by equations 2.21 and 2.22.

$$b \ll \sqrt{T_m K} \tag{2.21}$$

$$L \ll \frac{D_p^2}{4\pi^2\sqrt{T_m K}} \tag{2.22}$$

If the contributions of dimensionless rotor damping and leakage are much less than one, their dynamic contributions are negligible. See Appendix 1 for typical values of $\hat{b}$ and $\hat{L}$ for a 60 kW HST wind turbine indicating that these terms are negligible. This is expected to hold for a wide range of HST sizes and operating conditions.

2.4 Linearized Dynamics of $K\omega^2$-controlled Hydrostatic Wind Turbines

Lyapunov's indirect method is used to analyze the local stability for linear perturbations near the stationary point [17][18]. The linearized state equations given by Equations 2.23-2.25. For simplicity, the ^ notation is taken off dimensionless variables for the rest of the chapter.

$$\Delta\dot{\omega} = -\Delta\omega - \Delta p \tag{2.23}$$

$$\Delta\dot{p} = c^2(\Delta\omega - \Delta\alpha) \tag{2.24}$$

$$\Delta\dot{\alpha} = \psi(\Delta\alpha_{cmd} - \Delta\alpha) \tag{2.25}$$

The linearized expressions of the control law error in the pressure- and rotor speed-regulated systems are given by Equations 2.26 and 2.27.

$$\Delta e_{pr} = \Delta p - 2\Delta\omega \tag{2.26}$$

$$\Delta e_{rs} = \frac{1}{2}\Delta p - \Delta\omega \tag{2.27}$$

The pressure- and rotor speed-regulated systems discussed up to this point operate autonomously at the stationary point. We now introduce a perturbation in the aerodynamic torque ΔT as an external input in the dynamic equations. The non-autonomous pressure- and rotor speed-regulated systems are represented in the state space form:

$$\begin{bmatrix} \Delta\dot{\omega} \\ \Delta\dot{p} \\ \Delta\dot{\alpha} \end{bmatrix} = \begin{bmatrix} -1 & -1 & 0 \\ c^2 & 0 & -c^2 \\ -2K_p\psi & K_p\psi & -\psi \end{bmatrix} \begin{bmatrix} \Delta\omega \\ \Delta p \\ \Delta\alpha \end{bmatrix} + \begin{bmatrix} 1 \\ 0 \\ 0 \end{bmatrix} \Delta T \tag{2.28}$$

$$\begin{bmatrix} \Delta\dot{\omega} \\ \Delta\dot{p} \\ \Delta\dot{\alpha} \end{bmatrix} = \begin{bmatrix} -1 & -1 & 0 \\ c^2 & 0 & -c^2 \\ -K_p\psi & \frac{1}{2}K_p\psi & -\psi \end{bmatrix} \begin{bmatrix} \Delta\omega \\ \Delta p \\ \Delta\alpha \end{bmatrix} + \begin{bmatrix} 1 \\ 0 \\ 0 \end{bmatrix} \Delta T \tag{2.29}$$

The transfer functions for pressure-regulated P-control are:

$$\frac{\Omega_{\mathrm{pr}}(s)}{\Delta T(s)} = \frac{s^2 + \psi s + K_p c^2 \psi}{\mathit{\Delta}_{pr}(s)} \tag{2.35}$$

$$\frac{\mathrm{P}_{\mathrm{pr}}(s)}{\Delta T(s)} = c^2 \frac{s + \psi + 2K_p \psi}{\mathit{\Delta}_{pr}(s)} \tag{2.36}$$

$$\frac{\mathrm{A}_{pr}(s)}{\Delta T(s)} = -\frac{K_p \psi (2s - c^2)}{\mathit{\Delta}_{pr}(s)} \tag{2.37}$$

where the characteristic polynomial is

$$\mathit{\Delta}_{pr}(s) = s^3 + (1 + \psi)s^2 + \left(\psi + c^2 + K_p c^2 \psi\right)s + c^2\psi + 3K_p c^2 \psi \tag{2.38}$$

The transfers function for rotor speed-regulated P-control are:

$$\frac{\Omega_{\mathrm{rs}}(s)}{\Delta T(s)} = \frac{s^2 + \psi s + \frac{1}{2} K_p c^2 \psi}{\mathit{\Delta}_{rs}(s)} \tag{2.39}$$

$$\frac{\mathrm{P}_{\mathrm{rs}}(s)}{\Delta T(s)} = c^2 \frac{s + \psi + K_p \psi}{\mathit{\Delta}_{rs}(s)} \tag{2.40}$$

$$\frac{\mathrm{A}_{rs}(s)}{\Delta T(s)} = -\frac{K_p \psi (2s - c^2)}{\mathit{\Delta}_{rs}(s)} \tag{2.41}$$

where the characteristic polynomial is

$$\mathit{\Delta}_{rs}(s) = s^3 + (1 + \psi)s^2 + \left(\psi + c^2 + \frac{1}{2} K_p c^2 \psi\right)s + c^2\psi + \frac{3}{2} K_p c^2 \psi \tag{2.42}$$

Both systems have two zeros $z_{\omega 1}, z_{\omega 2} = f(K_p)$ in their rotor speed response and one zero $z_p = f(K_p)$ in their pressure response that are in the left half plane for $K_p > 0$. Both systems also have one zero $z_\alpha \neq f(K_p)$ in their swashplate response that is fixed in the right half plane. The stationary point (x_m, u_m) is locally asymptotically stable if the characteristic equations exclusively have roots in the left half plane (LHP) [24,25]. Conditions for these criteria are investigated in section 2.6.

2.5 Steady-State Control Law Error

The pressure- and rotor-speed regulated systems are both type zero so they will always have finite steady state control law error when tracking the stationary point. The systems' error transfer functions show how the error dynamics change with the controller gains.

$$\frac{\Delta E_{pr}(s)}{\Delta T(s)} = -\frac{(\psi + s)(2s - c^2)}{\Delta_{pr}(s)} \tag{2.43}$$

$$\frac{\Delta E_{rs}(s)}{\Delta T(s)} = -\frac{(\psi + s)(2s - c^2)}{\Delta_{rs}(s)} \tag{2.44}$$

This shows that both linearized systems have a fixed non-minimum phase zero regardless of the control gain K_p. The steady-state control law errors to a step perturbation torque ΔT are calculated using the final value theorem:

$$\Delta e_{pr}(\infty) = \frac{1}{3K_p + 1} \tag{2.45}$$

$$\Delta e_{rs}(\infty) = \frac{1}{3K_p + 2} \tag{2.46}$$

The steady-state error in both systems is approximately inversely proportional to K_p for large Kp. The difference between the two systems shrinks as K_p increases. $K_p > 33$ is required to achieve a desired 1% steady-state error in both systems.

2.6 Root Locus Analysis of Linearized P-Control Dynamics

Root locus is used to visualize how closed-loop systems poles and zeros vary with controller gain. Conventional root locus considers systems in Evan's form as in Figure 8.

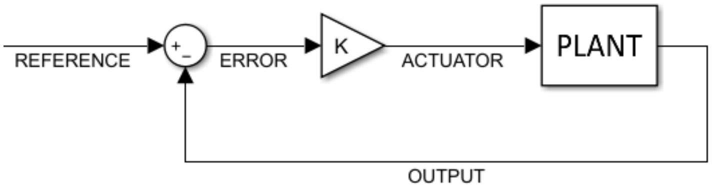

Figure 8. LTI system in Evan's form [25]

In Evan's form, the open-loop zeros remain unchanged as K varies. The linearized perturbation models of the pressure- and rotor speed-regulated systems are not in Evans' form so closed-loop poles and zeros both vary with loop gain. It is important to observe how the poles and zero move together. The transfer functions of the pressure-regulated system vary with control gain the same way as the transfer functions of the rotor speed-regulated system if $K_{p,rs} = 2K_{p,pr}$. This means that the two systems have different closed-loop poles and zeros for the same K_p but the root loci branches are identical between the pressure- and rotor speed-regulated systems. Figures 9-11 show root loci for the pressure-regulated systems. Open-loop poles are marked with an "X", and open-loop zeros are marked with an "O". Arrows along the branches show direction of increasing K_p. Both systems are linearized for 6 m/s wind by setting $c = 26$ and $\psi = 25$.

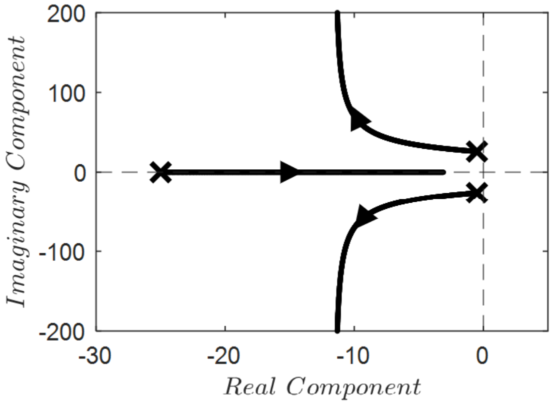

Figure 9. Pole root loci for pressure-regulated system with P-control

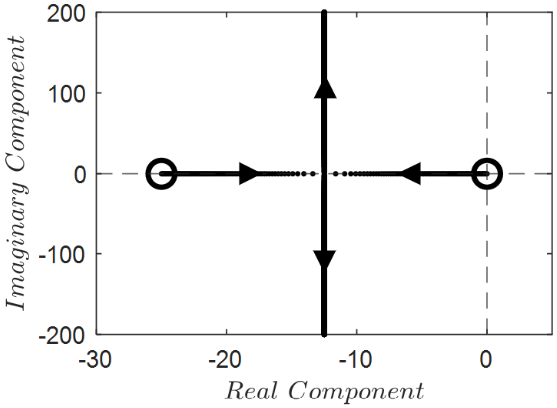

Figure 10. Rotor speed zero root loci for pressure-regulated system with P-control

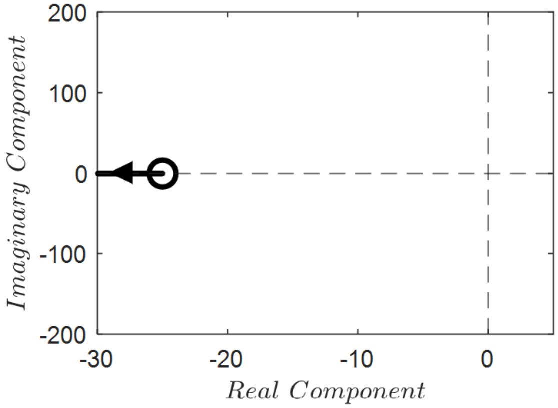

Figure 11. Pressure zero root loci for pressure-regulated system with P-control

The pole root locus of each system does not change for different outputs. The root loci for the rotor speed-regulated system are identical to those of the pressure-regulated system The closed-loop poles and zeros for both stay within the Left Half Plane (LHP) as K_p varies between $(0, \infty)$. The open-loop poles are comprised of a stable pair of complex conjugates and a fast stable real pole at $s = -\psi$. The closed-loop complex conjugates branch into the LHP before moving vertically away from the real axis. Regardless of K_p, the two complex poles have large imaginary components causing poorly damped response. The closed-loop real pole asymptotically approaches $s = -3$. Both systems are shown to be asymptotically stable because their poles are in the LHP, but the large imaginary components of the complex poles cause poorly damped response which is undesirable.

The open-loop rotor speed zeros are comprised of one at the origin and another at $s = -\psi$. The two closed-loop rotor speed zeros meet at $s = -\psi/2$ and diverge away from the real axis. The open-loop pressure zero starts at $s = -\psi$ and approaches $s = -\infty$. There is no meaningful interaction between these poles and zeros.

2.7 Conclusions about P-Controlled Systems

The dimensionless model simplifies analysis and understanding of $K\omega^2$-controlled hydrostatic wind turbines. They show that the hydrostatic transmission and swashplate response are much faster than the rotor response and show that rotor damping and leakage losses can be neglected for a 60-kW wind turbine. The root locus analysis shows how the closed-loop poles and zeros are affected by controller gain. Both pressure- and rotor speed-regulated systems have poorly damped responses regardless of K_p because the complex poles have large imaginary components. Adding an integrator to the controllers will improve steady-state error and provide another degree of freedom in shaping the root loci, but integral control is destabilizing.

3 Chapter 3: Analysis of PI-Controlled Linear Systems

3.1 $K\omega^2$ Law with Classical PI-control

The preceding chapter discusses using a classical P-controller to regulate either the HST wind turbine rotor speed or pressure. An integral term is added to the controller. This will eliminate steady-state error to a step input by increasing the system type but will be destabilizing. PI-control determines the command input using Equation 3.1:

$$\hat{\alpha}_{cmd} = \hat{K}_p \hat{e} + \hat{K}_i \int \hat{e} \tag{3.1}$$

Integrating the error introduces a new state raising the system order to four. For simplicity, the ^ notation is taken off for the rest of the chapter. Differentiating Equation 3.1 gives:

$$\dot{\alpha}_{cmd} = K_p \dot{\alpha} + K_i e \tag{3.2}$$

where e is the same as in chapter 2 and $\dot{e}$ is a nonlinear expression for error time derivative that differs for the pressure- and rotor speed-regulated systems.

$$\dot{e}_{pr} = c^2(\omega - \alpha) - 2 + 2a + 2a\omega^2 - 4a\omega + 2\omega p \tag{3.3}$$

$$\dot{e}_{rs} = \frac{c^2}{2\sqrt{p}}(\omega - \alpha) - \frac{1-a}{\omega} + a\omega - 2a + p - \Delta T \tag{3.4}$$

3.2 Linearized Dynamics of $K\omega^2$-controlled Hydrostatic Wind Turbines

Lyapunov's indirect method is used here to analyze the local stability for linear perturbations near the stationary point. The expressions for $\dot{\hat{e}}$ are linearized at the stationary point:

$$\Delta\dot{e}_{pr} = c^2(\Delta\omega - \Delta\alpha) + 2\Delta p + 2\Delta\omega - 2\Delta T \tag{3.5}$$

$$\Delta\dot{e}_{rs} = \frac{1}{2}\mathrm{c}^2\Delta\omega - \frac{1}{2}c^2\Delta\alpha + \Delta\omega + \Delta p - \Delta T \tag{3.6}$$

The pressure- and rotor speed-regulated systems discussed up to this point operate autonomously at the stationary point. We now introduce a perturbation in the aerodynamic torque ΔT as an external input in the dynamic equations. The non-autonomous pressure- and rotor speed-regulated systems are represented in the state space form:

$$\begin{bmatrix} \Delta\dot{\omega} \\ \Delta\dot{p} \\ \Delta\dot{\alpha} \\ \Delta\dot{\alpha}_{cmd} \end{bmatrix} = \begin{bmatrix} -1 & -1 & 0 & 0 \\ c^2 & 0 & -c^2 & 0 \\ 0 & 0 & -\psi & \psi \\ c^2K_p + 2K_p - 2K_i & 2K_p + K_i & -c^2K_p & 0 \end{bmatrix} \begin{bmatrix} \Delta\omega \\ \Delta p \\ \Delta\alpha \\ \Delta\alpha_{cmd} \end{bmatrix} + \begin{bmatrix} 1 \\ 0 \\ 0 \\ -2K_p \end{bmatrix} \Delta T \tag{3.7}$$

$$\begin{bmatrix} \Delta\dot{\omega} \\ \Delta\dot{p} \\ \Delta\dot{\alpha} \\ \Delta\dot{\alpha}_{cmd} \end{bmatrix} = \begin{bmatrix} -1 & -1 & 0 & 0 \\ c^2 & 0 & -c^2 & 0 \\ 0 & 0 & -\psi & \psi \\ \frac{1}{2}c^2K_p + K_p - K_i & K_p + \frac{1}{2}K_i & -\frac{1}{2}c^2K_p & 0 \end{bmatrix} \begin{bmatrix} \Delta\omega \\ \Delta p \\ \Delta\alpha \\ \Delta\alpha_{cmd} \end{bmatrix} + \begin{bmatrix} 1 \\ 0 \\ 0 \\ -K_p \end{bmatrix} \Delta T \tag{3.8}$$

The transfer functions for pressure-regulated PI-control are:

$$\frac{\Omega_{\mathrm{pr}}(s)}{\Delta T(s)} = \frac{s^3 + \psi s^2 + K_p c^2 \psi s + K_i c^2 \psi}{\Delta_{pr}(s)} \tag{3.9}$$

$$\frac{\mathrm{P_{pr}}(s)}{\Delta T(s)} = c^2 \frac{s^2 + (\psi + 2K_p\psi)s + 2K_i\psi}{\Delta_{pr}(s)} \tag{3.10}$$

$$\frac{\mathrm{A}_{pr}(s)}{\Delta T(s)} = \frac{-\psi(2s - c^2)(K_p s + K_i)}{\Delta_{pr}(s)} \tag{3.11}$$

$$\frac{\mathrm{A}_{cmd,pr}(s)}{\Delta T(s)} = \frac{-(s + \psi)(2s - c^2)(K_p s + K_i)}{\Delta_{pr}(s)} \tag{3.12}$$

where the characteristic polynomial is:

$$\Delta_{pr}(s) = s^4 + a_{3,pr}s^3 + a_{2,pr}s^2 + a_{1,pr}s + a_{0,pr} \tag{3.13}$$

$$a_{3,pr} = 1 + \psi$$

$$a_{2,pr} = \psi + c^2 + K_p c^2 \psi$$

$$a_{1,pr} = c^2\psi + K_i c^2 \psi + 3K_p c^2 \psi$$

$$a_{0,pr} = 3K_i c^2 \psi$$

The transfers function for rotor speed-regulated PI-control are:

$$\frac{\Omega_{\mathrm{rs}}(s)}{\Delta T(s)} = \frac{s^3 + \psi s^2 + \frac{1}{2}K_p c^2 \psi s + K_i c^2 \psi}{\Delta_{rs}(s)} \tag{3.14}$$

$$\frac{\mathrm{P_{rs}}(s)}{\Delta T(s)} = c^2 \frac{s^2 + (\psi + K_p\psi)s + K_i\psi}{\Delta_{rs}(s)} \tag{3.15}$$

$$\frac{\mathrm{A}_{rs}(s)}{\Delta T(s)} = \frac{-\psi(2s - c^2)(K_p s + K_i)}{\Delta_{rs}(s)} \tag{3.16}$$

$$\frac{\mathrm{A}_{cmd,rs}(s)}{\Delta T(s)} = \frac{-(s+\psi)(2s-c^2)\left(K_p s + K_i\right)}{\mathit{\Delta}_{rs}(s)} \tag{3.17}$$

where the characteristic polynomial is:

$$\mathit{\Delta}_{rs}(s) = s^4 + a_{3,rs}s^3 + a_{2,rs}s^2 + a_{1,rs}s + a_{0,rs} \tag{3.18}$$

$$a_{3,rs} = 1 + \psi$$

$$a_{2,rs} = \psi + c^2 + \frac{1}{2}K_p c^2 \psi$$

$$a_{1,rs} = c^2\psi + \frac{1}{2}K_i c^2 \psi + \frac{3}{2}K_p c^2 \psi$$

$$a_{0,rs} = \frac{3}{2}K_i c^2 \psi$$

The rotor speed, pressure and swashplate zeros vary with K_p and K_i. The controller zeros are the same as the swashplate zeros in addition to a fixed zero at $s = -\psi$. The stationary point (x_m, u_m) is locally asymptotically stable if the characteristic equations have roots in the left half plane (LHP). These criteria are investigated in section 3.4.

3.3 Steady-State Control Law Error

The pressure- and rotor-speed regulated systems with PI-control are both type one so they will always have zero steady state control law error when tracking a constant reference. The systems’ error transfer functions are:.

$$\frac{\Delta E_{pr}(s)}{\Delta T(s)} = -\frac{s(\psi+s)(2s-c^2)}{\Delta_{pr}(s)} \tag{3.19}$$

$$\frac{\Delta E_{rs}(s)}{\Delta T(s)} = -\frac{s(\psi + s)(2s - c^2)}{\Delta_{rs}(s)} \tag{3.20}$$

This shows that both linearized systems have a fixed non-minimum phase zero regardless of the control gains K_p and K_i. The steady-state control law errors to a step perturbation torque ΔT are calculated using the final value theorem:

$$\Delta e_{pr}(\infty) = \Delta e_{rs}(\infty) = 0 \tag{3.21}$$

The steady-state error for both systems tracking a constant reference is zero. So, steady-state error is not a design constraint with PI-control for a slowly-moving stationary point.

3.4 Root Locus Analysis of Linearized PI-Control Dynamics

Root locus is used to visualize how closed-loop systems poles and zeros vary with controller gain. The systems with PI-control are not in Evans' form so closed-loop poles and zeros both vary with loop gain. The PI-controlled systems here have two control degrees of freedom, K_p and K_i. $r_i = K_i/K_p$ that can be used to shape the loci. The transfer functions of the pressure-regulated system vary with control gain the same way as the transfer functions of the rotor speed-regulated system if $K_{p,rs} = 2K_{p,pr}$. This means that the two systems have different closed-loop poles and zeros for the same K_p but the root loci branches are identical between the pressure- and rotor speed-regulated systems. See Appendix 2 for pole and zero loci for various chosen values of r_i. Figures 12-14 show root loci for the pressure-regulated system with $r_i = 1$.

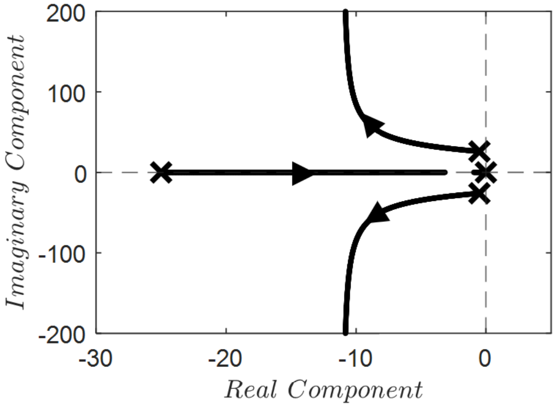

Figure 12. Pole root loci for pressure-regulated system with PI-control

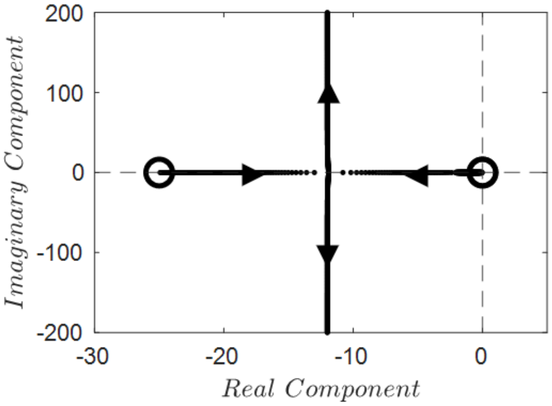

Figure 13. Rotor speed zero root loci for pressure-regulated system with PI-control

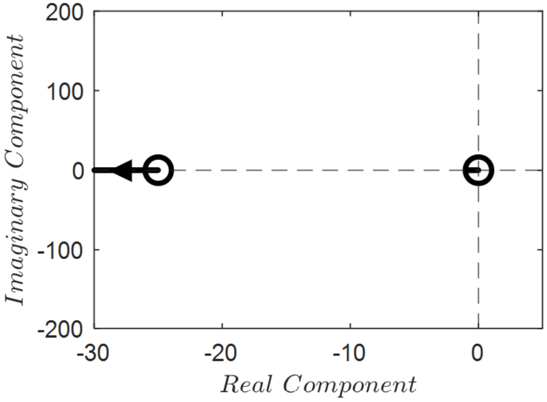

Figure 14. Pressure zero root loci for pressure-regulated system with PI-control

The root loci for the rotor speed-regulated system are identical to those of the pressure-regulated system. Both systems are asymptotically stable because their poles are all in the open LHP, but the large imaginary components of the complex poles cause poorly damped response. This is true for both pressure- and rotor speed-regulating systems.

3.5 Conclusions about PI-Controlled Systems

Including an integrator in the controller improved steady-state error and gave more design flexibility for the PI-controlled systems. However, this new design flexibility does not draw the complex poles closer to the negative real axis. This shows it is not feasible to achieve a reasonably-damped response for the PI-controlled systems. Adding a differentiating component to the controllers adds another degree of freedom to shape the root loci and improves damping.

4 Chapter 4: Analysis of PID-Controlled Linear Systems

4.1 $K\omega^2$ Law with Classical PID-control

The preceding chapter discusses using a classical PI-controller to regulate the HST wind turbine rotor speed or pressure. This improved steady-state error but reduced damping. A derivative term to the controller to stabilize the transient response. PID-control determines the command input using Equation 4.1.

$$\alpha = K_p e + K_i \int e + K_d \dot{e} \tag{4.1}$$

Equation 4.2 expresses the integrator dynamics by rearranging (4.1) as

$$\dot{\alpha} = K_p \dot{e} + K_i e + K_d \ddot{e} \tag{4.2}$$

where e and $\dot{e}$ are the same as in chapters 2 and 3 and $\ddot{e}$ is a nonlinear expression that is different for the pressure- and rotor speed-regulated systems.

$$\begin{aligned}\ddot{e}_{pr} = {} & 4a - 4a\Delta T + 2\Delta T p + 8ap + \Delta T c^2 + 2ac^2 - c^2 p - \frac{4a}{\omega} + 12a^2\omega + \frac{2p}{\omega} - 12a^2 \\ & - 2p^2 + \frac{4a^2}{\omega} - 4a^2\omega^2 + \frac{c^2}{\omega} + 2c^2\omega^2 - \frac{2ap}{\omega} - \frac{ac^2}{\omega} + 4\Delta T a\omega - 6ap\omega + \alpha c^2 \psi \\ & -\alpha_{cmd} c^2 \psi - ac^2\omega - 2\alpha c^2 \omega \end{aligned} \tag{4.3}$$

$$\begin{aligned}\ddot{e}_{rs} = {} & \Delta T a - ap - \alpha c^2 + \frac{\Delta T}{\omega^2} + \frac{2a}{\omega^2} - a^2\omega - \frac{2a}{\omega^3} + c^2\omega - \frac{\hat{p}}{\omega^2} + 2a^2 + \frac{1}{\omega^3} - \frac{c^2 p^{\frac{1}{2}}}{2} \\ & - \frac{2a^2}{\omega^2} + \frac{a^2}{\omega^3} + \frac{ap}{\omega^2} + \frac{\Delta T c^2}{2p^{\frac{1}{2}}} + \frac{ac^2}{p^{\frac{1}{2}}} - \frac{\alpha^2 c^4}{4p^{\frac{3}{2}}} + \frac{c^2}{2p^{\frac{1}{2}}\omega} - \frac{c^4\omega^2}{4p^{\frac{3}{2}}} - \frac{\Delta T a}{\omega^2} - \frac{ac^2}{2p^{\frac{1}{2}}\omega} + \frac{\alpha c^2 \psi}{2p^{\frac{1}{2}}} \end{aligned}$$

$$-\frac{\alpha_{cmd}c^2\psi}{2p^{\frac{1}{2}}} - \frac{ac^2\omega}{2p^{\frac{1}{2}}} + \frac{\alpha c^4\omega}{2p^{\frac{3}{2}}} \tag{4.4}$$

4.2 Linearized Dynamics of $K\omega^2$-controlled Hydrostatic Wind Turbines

Lyapunov's indirect method is also used here to analyze the local stability for linear perturbations near the stationary point. The linearized controller dynamic equation is

$$\Delta\dot{\alpha}_{cmd} = K_d\Delta\ddot{e} + K_p\Delta\dot{e} + K_i\Delta e \tag{4.5}$$

where expressions for $\ddot{e}$ are linearized at the stationary point m.

$$\Delta\ddot{e}_{pr} = 2\Delta T - 2\Delta p - 2\Delta\omega + \Delta T c^2 - 2c^2\Delta\alpha - c^2\Delta p + c^2\Delta\omega + c^2\Delta\alpha\psi - c^2\Delta\alpha_{cmd}\psi \tag{4.6}$$

$$\Delta\ddot{e}_{rs} = \Delta T - \Delta p - \Delta\omega + \frac{1}{2}c^2\Delta T - c^2\Delta\alpha + \frac{1}{2}c^2\Delta\omega - \frac{1}{2}c^2\Delta p + \frac{1}{2}c^2\psi\Delta\alpha - \frac{1}{2}c^2\psi\Delta\alpha_{cmd} \tag{4.7}$$

The pressure- and rotor speed-regulated systems discussed up to this point operate autonomously at the stationary point. We now introduce a perturbation in the aerodynamic torque ΔT as an external input in the dynamic equations. The non-autonomous pressure- and rotor speed-regulated systems are represented in the state space form:

$$\begin{bmatrix} \Delta\dot{\omega} \\ \Delta\dot{p} \\ \Delta\dot{\alpha} \\ \Delta\dot{\alpha}_{cmd} \end{bmatrix} = \begin{bmatrix} -1 & -1 & 0 & 0 \\ c^2 & 0 & -c^2 & 0 \\ 0 & 0 & -\psi & \psi \\ a_{41,pr} & a_{42,pr} & a_{43,pr} & a_{44,pr} \end{bmatrix} \begin{bmatrix} \Delta\omega \\ \Delta p \\ \Delta\alpha \\ \Delta\alpha_{cmd} \end{bmatrix} + \begin{bmatrix} 1 \\ 0 \\ 0 \\ -2K_p + c^2K_d + 2K_d \end{bmatrix} \Delta T \tag{4.8}$$

$$a_{41,pr} = c^2\left(K_p + K_d\right) + 2\left(K_p - K_i - K_d\right), \qquad a_{42,pr} = 2\left(K_p - K_d\right) + K_i - c^2K_d$$

$$a_{43,pr} = c^2\left(\psi K_d - 2K_d - K_p\right), \qquad a_{44,pr} = -c^2\psi K_d$$

$$\begin{bmatrix} \Delta\dot{\omega} \\ \Delta\dot{p} \\ \Delta\dot{\alpha} \\ \Delta\dot{\alpha}_{cmd} \end{bmatrix} = \begin{bmatrix} -1 & -1 & 0 & 0 \\ c^2 & 0 & -c^2 & 0 \\ 0 & 0 & -\psi & \psi \\ a_{41,rs} & a_{42,rs} & a_{43,rs} & a_{44,rs} \end{bmatrix} \begin{bmatrix} \Delta\omega \\ \Delta p \\ \Delta\alpha \\ \Delta\alpha_{cmd} \end{bmatrix} + \begin{bmatrix} 1 \\ 0 \\ 0 \\ -K_p + \frac{1}{2}c^2\,K_d + K_d \end{bmatrix} \Delta T \qquad (4.9)$$

$$a_{41,rs} = c^2\left(\frac{1}{2}K_p + \frac{1}{2}K_d\right) + K_p - K_i - K_d, \qquad a_{42,rs} = K_p - K_d + \frac{1}{2}K_i - \frac{1}{2}K_d c^2$$

$$a_{43,rs} = c^2\left(\frac{1}{2}K_d\psi - K_d - \frac{1}{2}K_p\right), \qquad a_{44,rs} = -\frac{1}{2}K_d c^2\psi$$

The transfer functions for pressure-regulated PID-control are:

$$\frac{\Omega_{\mathrm{pr}}(s)}{\Delta\tau_{aero}(s)} = \frac{s^3 + (\psi + K_d c^2\psi)s^2 + \left(2K_d c^2\psi + K_p c^2\psi\right)s + K_i c^2\psi}{\Delta_{pr}(s)} \qquad (4.10)$$

$$\frac{\mathrm{P}_{\mathrm{pr}}(s)}{\Delta\tau_{aero}(s)} = c^2\,\frac{s^2 + \left(\psi - 2K_d\psi + 2K_p\psi\right)s + 2K_i\psi}{\Delta_{pr}(s)} \qquad (4.11)$$

$$\frac{\mathrm{A}_{pr}(s)}{\Delta\tau_{aero}(s)} = \psi\,\frac{\left(2K_d - 2K_p + K_d c^2\right)s^2 + \left(K_p c^2 - 2K_i + 2K_d c^2\right)s + K_i c^2}{\Delta_{pr}(s)} \qquad (4.12)$$

$$\frac{\mathrm{A}_{cmd,pr}(s)}{\Delta\tau_{aero}(s)} = (s + \psi)\,\frac{\left(2K_d - 2K_p + K_d c^2\right)s^2 + \left(K_p c^2 - 2K_i + 2K_d c^2\right)s + K_i c^2}{\Delta_{pr}(s)} \qquad (4.13)$$

Where the characteristic polynomial is

$$\Delta_{\mathrm{pr}}(s) = s^4 + a_{3,pr}s^3 + a_{2,pr}s^2 + a_{1,pr}s + a_{0,pr} \qquad (4.14)$$

$$a_{3,pr} = \psi + 1 + K_d c^2, \qquad \psi a_{2,pr} = \psi + c^2 + 3K_d c^2\psi + K_p c^2\psi$$

$$a_{1,pr} = c^2\psi + K_i c^2\psi + 3K_p c^2\psi, \qquad a_{0,pr} = 3K_i c^2\psi$$

The transfer functions for rotor speed-regulated PID-control are;

$$\frac{\Omega_{\mathrm{rs}}(s)}{\Delta\tau_{aero}(s)} = \frac{2s^3 + (2\psi + K_d c^2\psi)s^2 + \left(2K_d c^2\psi + K_p c^2\psi\right)s + K_i\, c^2\psi}{\Delta_{rs}(s)} \tag{4.15}$$

$$\frac{\mathrm{P}_{\mathrm{rs}}(s)}{\Delta\tau_{aero}(s)} = 2c^2\,\frac{s^2 + \left(\psi\ - K_d\psi + K_p\psi\right)s + K_i\psi}{\Delta_{rs}(s)} \tag{4.16}$$

$$\frac{\mathrm{A}_{rs}(s)}{\Delta\tau_{aero}(s)} = \psi\,\frac{\left(2K_d - 2K_p + K_d c^2\right)s^2 + \left(K_p c^2 - 2K_i + 2K_d c^2\right)s + K_i c^2}{\Delta_{rs}(s)} \tag{4.17}$$

$$\frac{\mathrm{A}_{cmd,rs}(s)}{\Delta\tau_{aero}(s)} = (s+\psi)\,\frac{\left(2K_d - 2K_p + K_d c^2\right)s^2 + \left(K_p c^2 - 2K_i + 2K_d c^2\right)s + K_i c^2}{\Delta_{rs}(s)} \tag{4.18}$$

Where the characteristic polynomial is

$$\Delta_{\mathrm{rs}}(s) = s^4 + a_{3,rs}s^3 + a_{2,rs}s^2 + a_{1,rs}s + a_{0,rs} \tag{4.19}$$

$$a_{3,rs} = \psi\ +\ 1 + \frac{1}{2}K_d c^2\psi, \qquad \psi a_{2,rs} = \psi\ \ +\ c^2\ + \frac{3}{2}K_d c^2\psi\ +\ \frac{1}{2}K_p c^2\psi$$

$$a_{1,rs} = c^2\psi\ \ + \frac{1}{2}K_i c^2\psi\ + \frac{3}{2}\ K_p c^2\psi, \qquad a_{0,rs} = \frac{3}{2}K_i c^2\psi$$

The rotor speed, pressure and swashplate zeros vary with K_p and K_i. Remarkably, all transfer functions are identical for the pressure- and rotor speed-regulated systems if $K_{p,rs} = 2K_{p,pr}$, $K_{i,rs} = 2K_{i,pr}$ and $K_{d,rs} = 2K_{d,pr}$. The controller zeros are the same as the swashplate zeros in addition to a fixed zero at $s = -\psi$. The stationary point (x_m, u_m) is locally asymptotically stable if the characteristic equations exclusively have roots in the left half plane (LHP). These criteria are investigated in section 4.4.

4.3 Steady-State Control Law Error

The pressure- and rotor-speed regulated systems with PID-control are both type one so they will always have zero steady state control law error when tracking a constant reference. The systems' error transfer functions show how the error changes with time.

$$\frac{\Delta E_{pr}(s)}{\Delta T(s)} = -\frac{s[2s^2 + (2\psi - c^2 + 2K_d c^2\psi)s - c^2\psi + 6K_d c^2\psi]}{\Delta_{\mathrm{pr}}(s)} \qquad (4.20)$$

$$\frac{\Delta E_{rs}(s)}{\Delta T(s)} = -\frac{s[\,2s^2 + (2\psi + K_d c^2\psi - c^2)s + 3K_d c^2\psi - c^2\psi\,]}{\Delta_{\mathrm{rs}}(s)} \qquad (4.20)$$

Both linearized systems have a fixed non-minimum phase zero regardless of the control gains K_p and K_i. The steady-state control law errors to a step perturbation torque ΔT are calculated using the final value theorem:

$$\Delta e_{pr}(\infty) = \Delta e_{rs}(\infty) = 0 \qquad (4.21)$$

The steady-state error for both systems tracking a constant reference is zero. So, steady-state error is no longer a design constraint with PID-control so long as the stationary point is constant or slow-moving.

4.4 Root Locus Analysis of Linearized PID-control Dynamics

Root locus is used to visualize how closed-loop systems' poles and zeros vary with controller gain. The systems with PID-control are also not in Evans' form so closed-loop poles and zeros both vary with loop gain. The PID-controlled systems here have three control degrees of freedom: K_p, K_i and K_d. $r_i = K_i/K_p$ and $r_d = K_d/K_p$ are used to shape the loci to reach closed-loop pole and zero locations with desirable characteristics. The transfer functions of the pressure -regulated system vary with control gain the same way as the transfer functions of the rotor speed-regulated system if $K_{p,rs} = 2K_{p,pr}$. This means that the two systems have different closed-loop poles and zeros for the same K_p but the root loci branches are identical between the pressure- and rotor speed-regulated systems. See Appendix 3 for pole loci for chosen pairs of r_i and r_d. $r_i = 5$ and $r_d = 0.1$ are selected because the complex conjugate branches are near the axis while far from the origin resulting in well-damped response of the complex poles and fast response time of the dominant real pole.

The next step is to investigate how to achieve the design objectives with a particular value of K_p by moving the closed-loop poles along the selected loci. Figure 14 shows one configuration of pole loci for $r_i = 5$ and $r_d = 0.1$ for the PR- and RS-regulated systems. Pole branches are black and poles at chosen values of K_p are marked with an “X” for $K_p = 0$, a hexagram for $K_p = 0.01$, a square for $K_p = 0.1$, a diamond for $K_p = 1$, a triangle for $K_p = 2$ and a pentagram for $K_p = 5$.

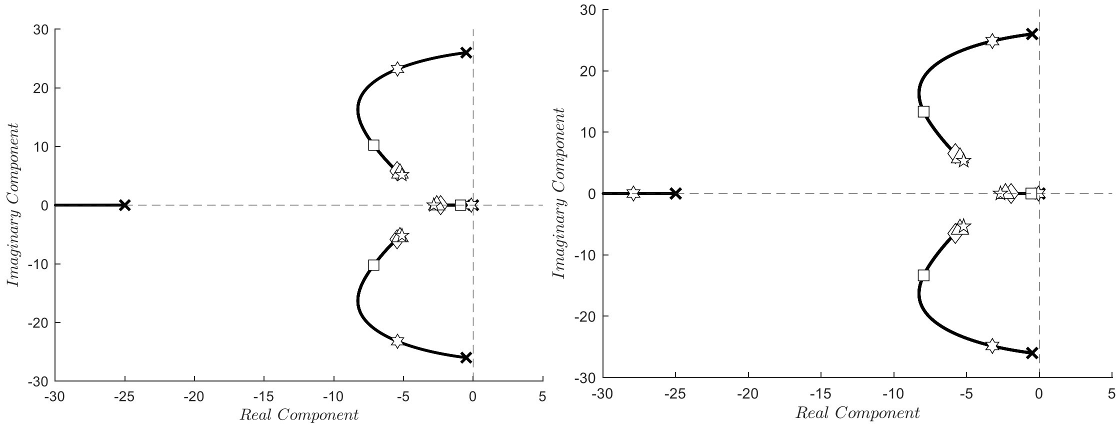

Figure 15. Pole root loci of pressure- regulated (left) and rotor speed-regulated (right) systems with PID-control for $r_i = 5$ and $r_d = 0.1$

Both systems with PID-control draw the complex pole branches toward the real axis and draw the pole beginning at the origin toward $s = -3$. This dominant pole limits the speed of response for both systems. Poles approach the asymptotic locations for $K_p > 0.1$. Thus, both systems are not sensitive to variation for $K_p > 0.1$. $K_{p,pr} = 5$ and $K_{p,rs} = 10$ gives dominant poles at $s = -2.8289, -5.1030 \pm 5.1813i$ and an effective damping ratio of 0.7. Although this is not an archetypal second-order system, tuning for a high damping ratio gives a well-damped response. The next step is to investigate how the zeros interact with the pole root locus. Figure 16 shows rotor speed zero root loci for the pressure- and rotor speed-regulated systems with $r_i = 5$ and $r_d = 0.1$. Figure 17 shows pressure zero root loci for the pressure- and rotor speed-regulated systems with $r_i = 5$ and $r_d = 0.1$.

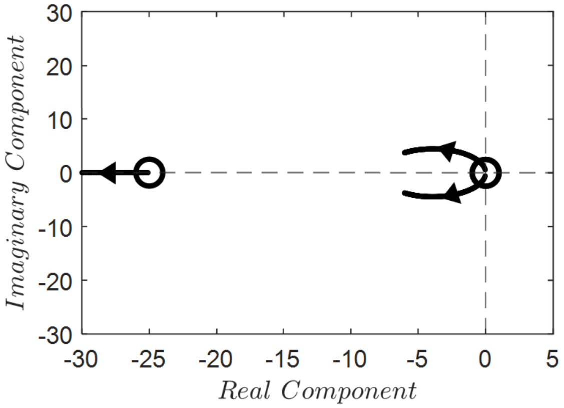

Figure 16. Rotor speed zero root loci for pressure-regulated system with PID-control for $r_i = 5$, $r_d = 0.1$

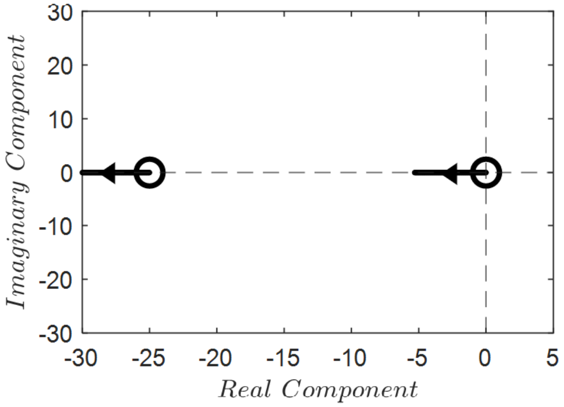

Figure 17. Pressure zero root loci for pressure-regulated system with PID-control for $r_i = 5$, $r_d = 0.1$

The zero root loci for the rotor speed-regulated system are identical to those of the pressure-regulated system. The zero loci for all responses cross over the pole loci. The closed-loop poles and zeros for $K_{p,pr} = 5$, $K_{p,rs} = 10$, $r_i = 5$ and $r_d = 0.1$ are shown in Figure 18.

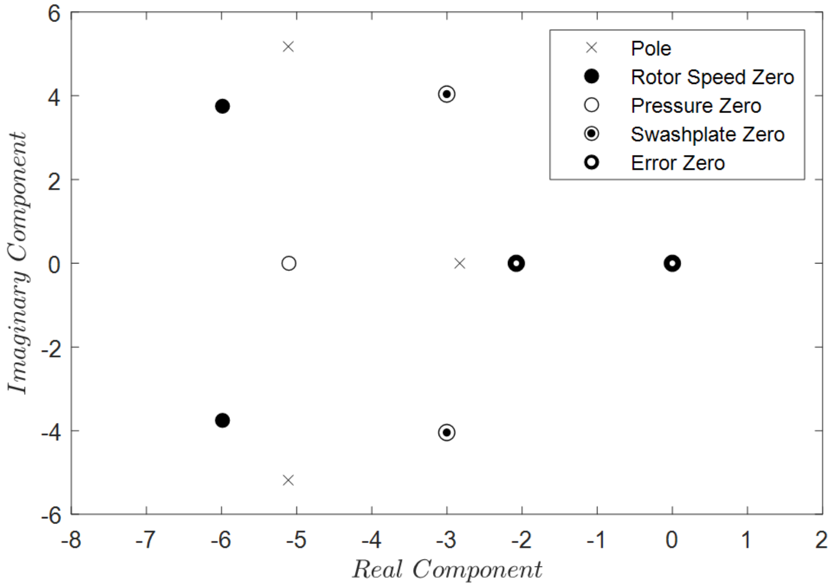

Figure 18. Closed-loop poles and zeros for $K_{p,pr} = 5$, $K_{p,rs} = 10$, $r_i = 5$ and $r_d = 0.1$

This excludes the fast real poles and zeros far from the origin. The complex rotor speed zeros are close to the complex poles, but real pressure zeros are not. See Equations (4.22) and (4.23) below.

$$\frac{\Omega(s)}{\Delta T(s)} = \frac{(s + 5013)(s^2 + 11.96s + 49.87)}{(s + 5013)(s + 2.829)(s^2 + 10.21s + 52.89)} \tag{4.22}$$

$$\frac{\mathrm{P}(s)}{\Delta T(s)} = \frac{(s + 244.9)(s + 5.104)}{(s + 5013)(s + 2.829)(s^2 + 10.21s + 52.89)} \tag{4.23}$$

$$\frac{\mathrm{A}(s)}{\Delta T(s)} = \frac{s^2 + 6.01s + 25.58}{(s + 5013)(s + 2.829)(s^2 + 10.21s + 52.89)} \tag{4.24}$$

$$\frac{E(s)}{\Delta T(s)} = \frac{s(s + 4823)(s + 2.073)}{(s + 5013)(s + 2.829)(s^2 + 10.21s + 52.89)} \tag{4.25}$$

The rotor speed response is dominated by a stable real pole. The pressure response does not have complex zeros to mitigate the effects of the complex poles so there will be fast oscillations. The swashplate response has complex zeros that will partially mitigate the effects of the complex poles. The error response has a real zero to partially mitigate the real pole so the error will have a faster but more oscillatory response.

4.5 Conclusions about PID-controlled Systems

Adding a differentiating component to the classical controllers makes it possible to shape the loci to bend complex branches toward the real axis. Selecting the PID gains as $K_{p,pr} = 5$, $K_{p,rs} = 10$, $r_i = 5$ and $r_d = 0.1$ gives both the pressure- and rotor speed-regulated systems a well-damped and fast response. Complex poles are partially cancelled by rotor speed zeros but not pressure zeros which will affect how the pressure- and rotor speed-regulated systems track their respective references. Both systems are proposed as viable methods of HST wind turbine Region 2 control.

5 Chapter 5: Numerical Simulations of Scaled Nonlinear Models

The preceding root locus analysis is limited to small linear perturbations from the stationary point. Parameters are dimensionless unless stated otherwise. The study is extended to investigate the nonlinear pressure- and rotor speed-regulated system performance for larger perturbations and varying control gain K. Numerical models of the two systems were developed in MATLAB ® Simulink.

5.1 Simulation Results and Discussion

Controller performance under ideal conditions with $K = K_{ideal}$, under varying power characteristic curvature a , and under varying control law gain K is studied. State responses are observed to monitor transient behavior of the system. Error response is observed to compare control MPPT tracking. Power response is observed to compare steady-state power capture performance.

5.1.1 Ideal Conditions Study

The first step is to investigate how the proposed nonlinear systems track a stationary point when initialized there. The stationary point is selected to be at 6 m/s with $c = 26$. The dimensionless state and power responses of both proposed systems under this condition are compared in Figure 19.

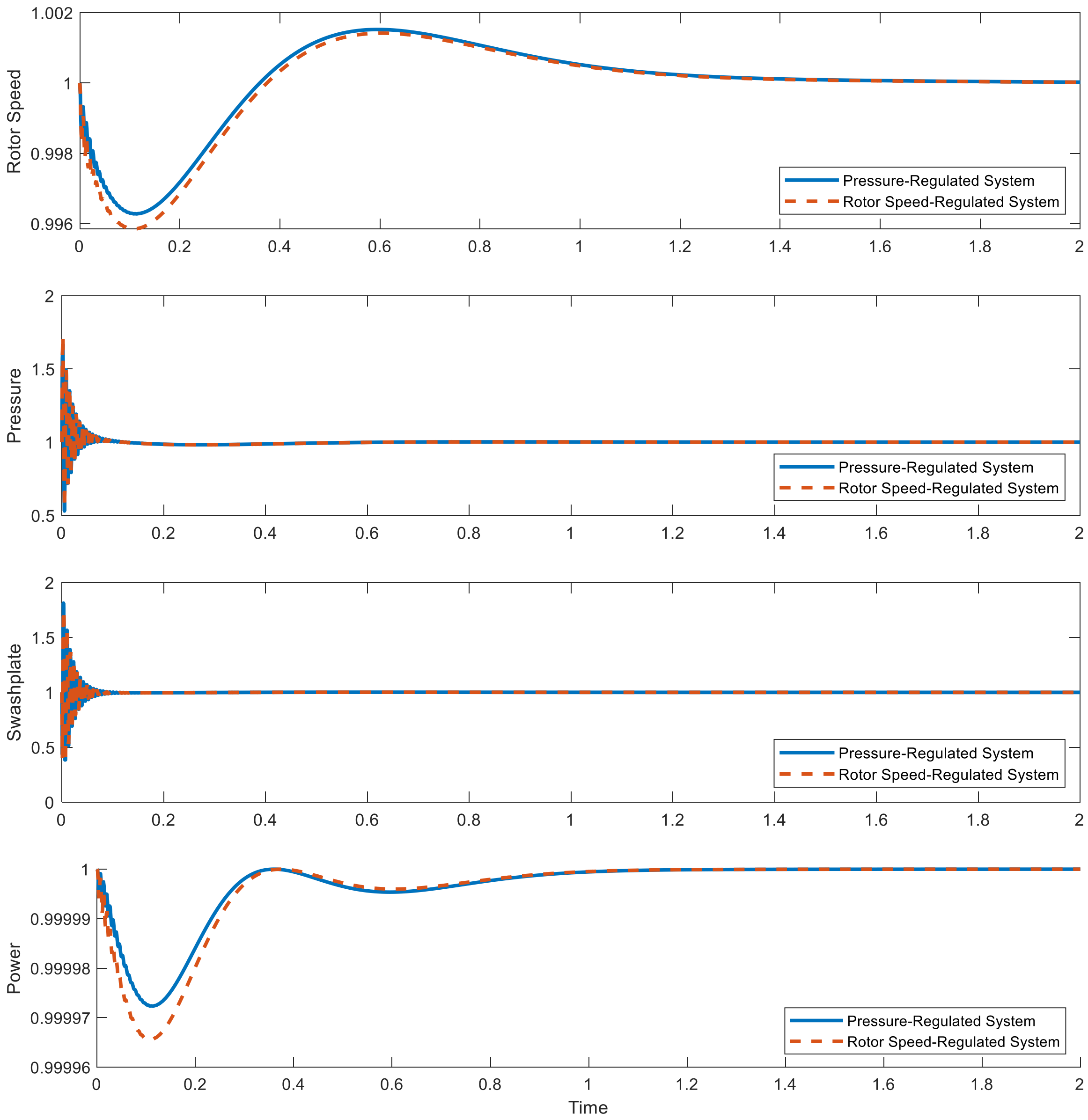

Figure 19. Dimensionless state and power time responses of systems initialized at the stationary point.

This shows that differences in power capture between the proposed systems are negligible. Both PID-controlled systems perfectly track the stationary point.

The second step is to investigate how the proposed nonlinear systems track the stationary point when initialized away from the stationary point. Two different initial conditions are investigated. First, states are arbitrarily initialized at $\Delta\omega = \Delta p = \Delta\alpha = \Delta\alpha_{cmd} = \Delta T =$

0.5. Figure 20 shows the dimensionless state and power time responses of the pressure- and rotor speed-regulated systems initialized under these conditions.

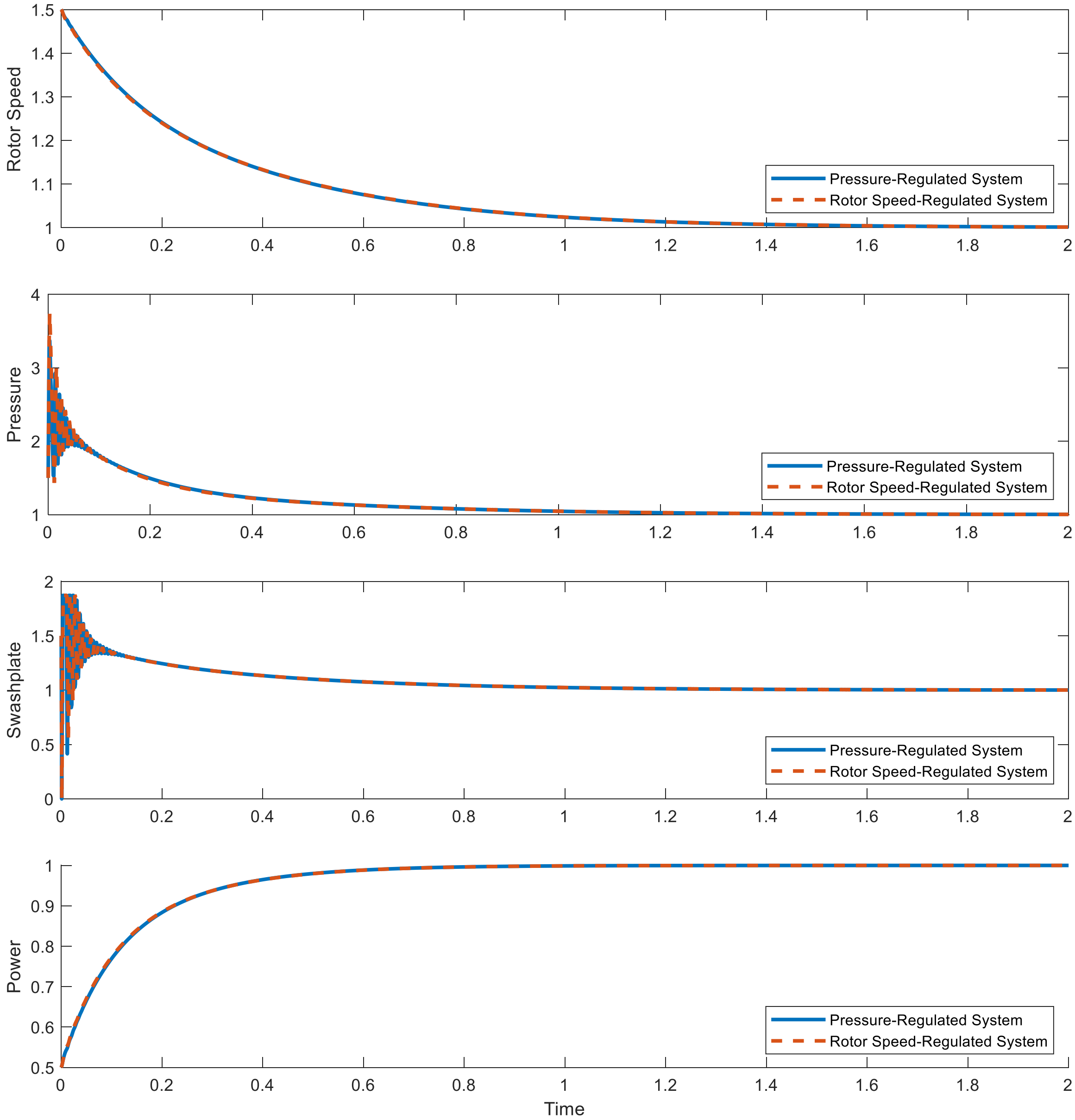

Figure 20. Dimensionless state and power time responses of systems initialized arbitrarily away from the stationary point.

Figure 21 shows phase portraits of the dimensionless rotor speed and pressure responses of the pressure- and rotor speed-regulated systems initialized under the same conditions.

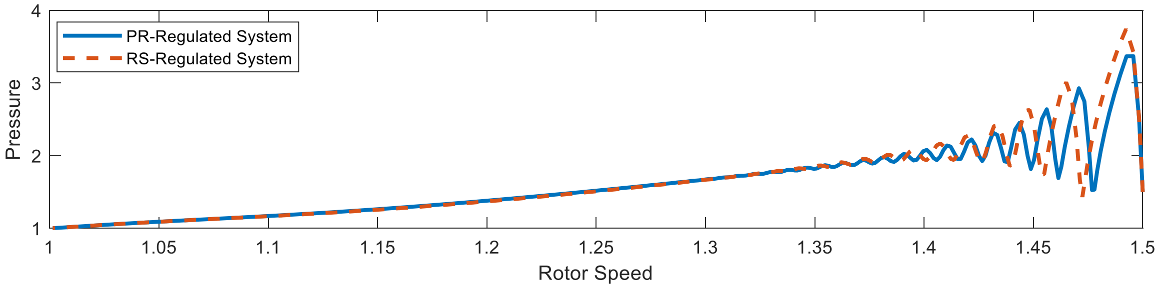

Figure 21. Phase portrait of rotor speed and pressure responses of systems initialized arbitrarily away from the stationary point.

Next, states are arbitrarily initialized to reflect initial steady operation at 5 m/s wind before moving to the stationary point at 6 m/s wind. Appendix 1 shows how the initial conditions are calculated. Figure 22 shows the dimensionless state and power time responses of the pressure- and rotor speed-regulated systems initialized at 6 m/s wind.

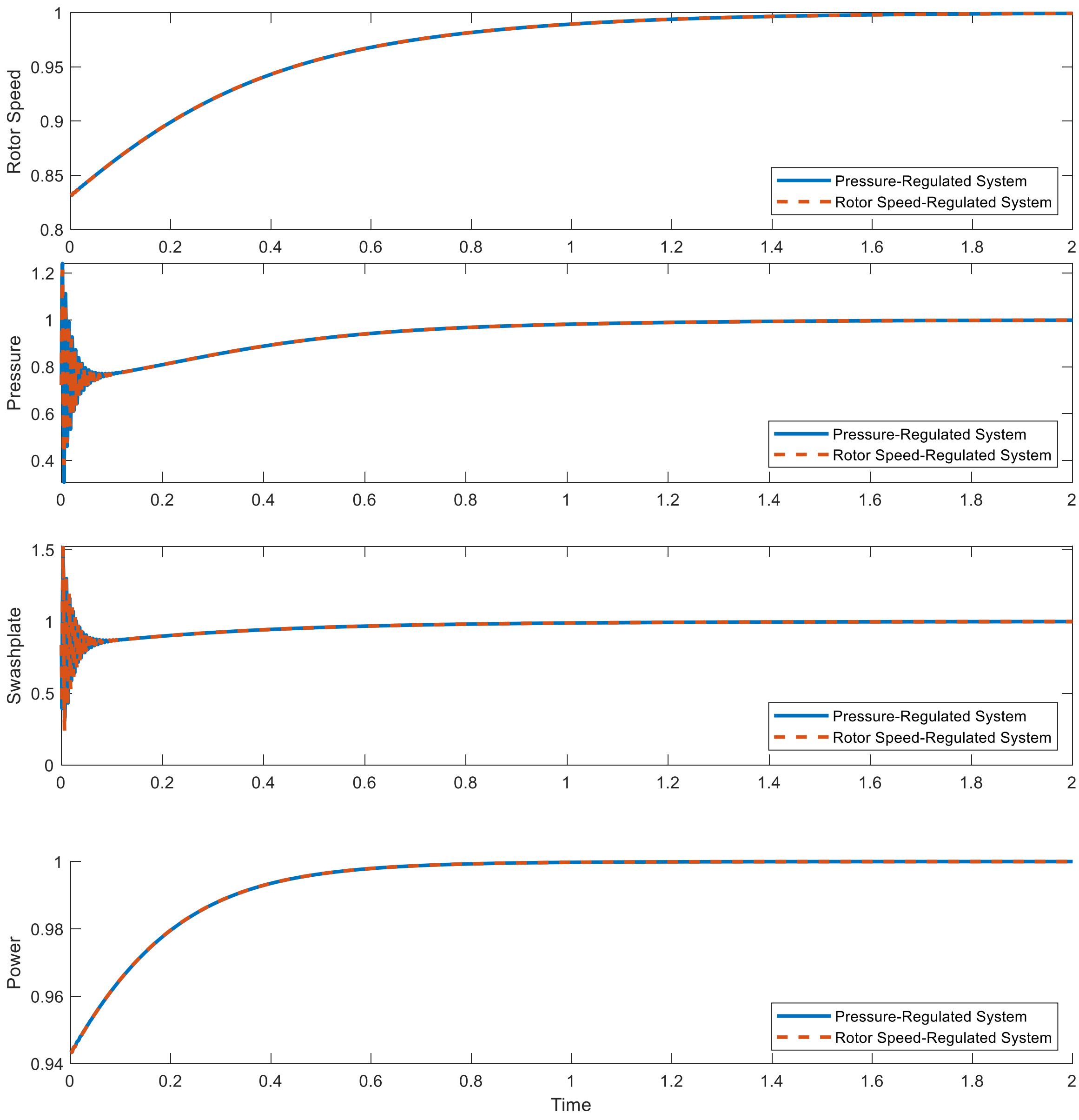

Figure 22. Dimensionless state and power time responses of systems initialized away from the stationary point to reflect initial operation at 5 m/s wind.

Figure 23 shows phase portraits of the dimensionless rotor speed and pressure responses of the pressure- and rotor speed-regulated systems initialized under the same conditions.

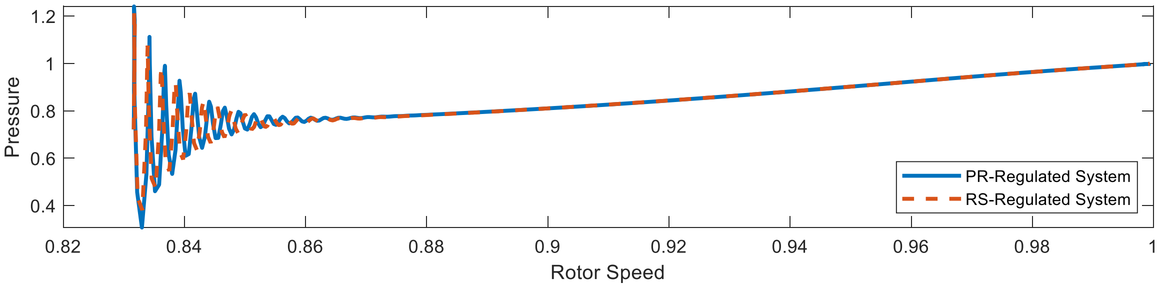

Figure 23. Phase portrait of rotor speed and pressure responses of systems initialized away from the stationary point to reflect initial operation at 5 m/s wind.

Both systems first oscillate and then smoothly converge to the stationary point regardless of the physically realizable initial conditions. This behavior is consistent for a large span of realistic initial conditions. However, note that the actuator briefly saturates at $\hat{\alpha}_{max} = 1.87$ for both systems when they are initialized arbitrarily. The initial fast oscillations in the pressure response are caused by the complex poles. The rotor speed response is less oscillatory because the rotor speed zeros are close to the complex poles and mitigate their effects. This study shows that the linearized models for both pressure- and rotor speed regulated systems are accurate for a wide range of operating conditions. Further, the pressure- and rotor speed-regulated systems are locally asymptotically stable and the modeled nonlinearities do not cause significant differences in the two systems' behavior for the perturbations studied.

5.1.2 Effect of Variation in a

The second step is to investigate how varying a affects the transient behavior of the pressure- and rotor speed-regulated systems. For a 60 kW wind turbine, $a = 2$ is a realistic value. The curvature will have varying degrees of effect when the systems are operating at and away from the stationary point. The stationary point is selected to be at 6 m/s. This is reflected by selecting $c = 26$. The dimensionless power responses of both proposed systems under this condition are compared in Figure 24.

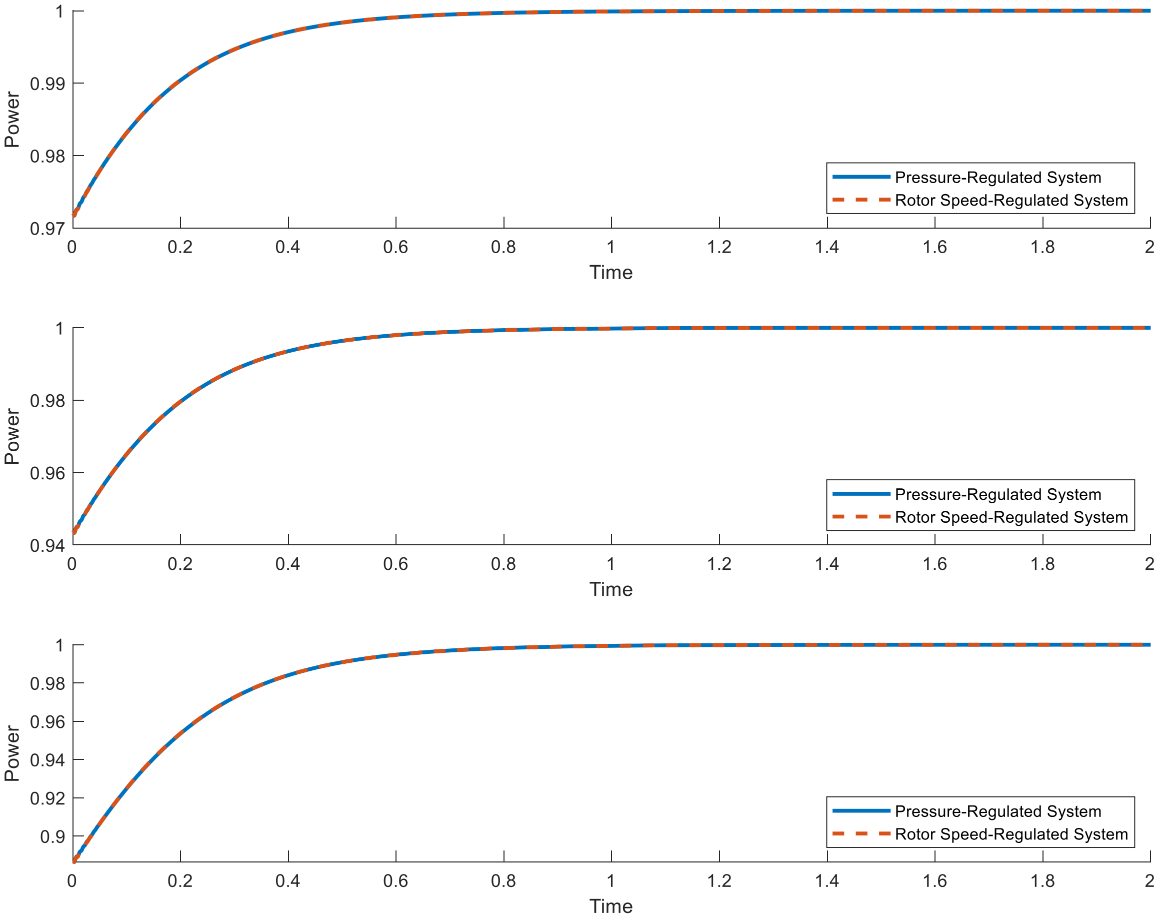

Figure 24. Dimensionless power responses of systems with a = 1 (top), a=2 (middle) and a=4 (bottom)

Varying a changes how much power is captured for a fixed rotor speed away from the stationary point. As a increases, the local power characteristic gradient increases which makes the systems more sensitive to variation in operating conditions away from the stationary point. This is evident in the above results where the initial power capture away from the stationary point decreases as a increases.

5.1.3 Studying Effect of Variation in K at the Stationary Point

The next step is to investigate the effect of varying the control law gain K on steady power capture. The pressure- and rotor speed-regulated systems are steadily operated at the stationary point and tested for various values of the control law gain K. The stationary point at a steady 6 m/s wind is reflected by valuing $c = 26$. $K_{ideal} = 1$ aligns with the power characteristic which has a local peak at $\omega = 1$. Figure 25 shows how power capture varies with K.

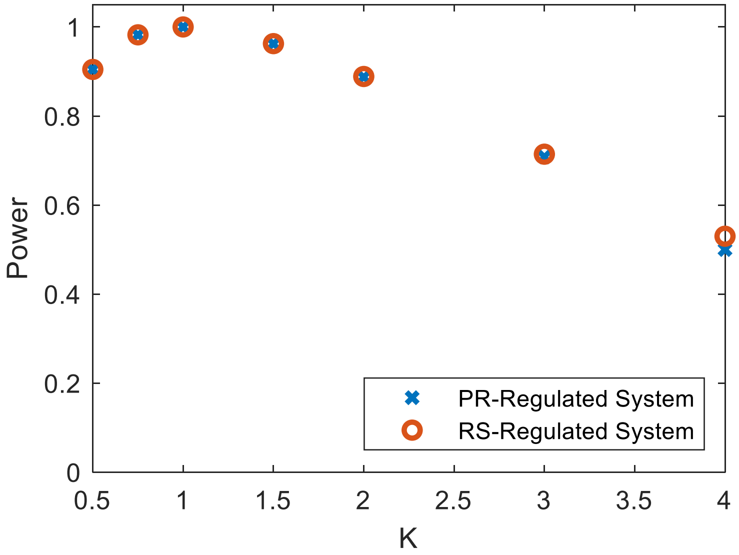

Figure 25. Power capture with variation in K

The systems experience nearly identical power losses for $K \neq 1$. These power losses increase as K moves away from its optimal value of one. The modeled nonlinearities do not cause significant differences in the two systems' robustness to variations in K.

5.2 Conclusions from the Simulation Study

The pressure- and rotor speed- systems perform comparably regardless of the nonlinear differences between the two $K\omega^2$ control laws. The systems share smooth, well-damped behavior like that of a first-order linear system. The systems are robust to realistic variations in the curvature a of the power characteristic but experience reduction in power capture when subject to variations in the control law gain K.

6 Chapter 6: Hardware-in-the-Loop Experiments on the Control of Hydrostatic Transmission Wind Turbines

The dimensionless simulation study does not include energy loss terms, component efficiencies, and unmodeled nonlinearities in the hardware. To study these effects, Hardware-In-the-Loop (HIL) experiments were conducted using the HST Test Stand at the University of Minnesota.

6.1 Test Stand at the University of Minnesota – Twin Cities

The test stand at the University of Minnesota is shown in Figure 26. The hydrostatic drive (HSD) on the right loads the rotor shaft to emulate wind effects for the HST on the left. The power output on HST high speed shaft feeds to the variable frequency drive (VFD) which helps power the hydrostatic drive.

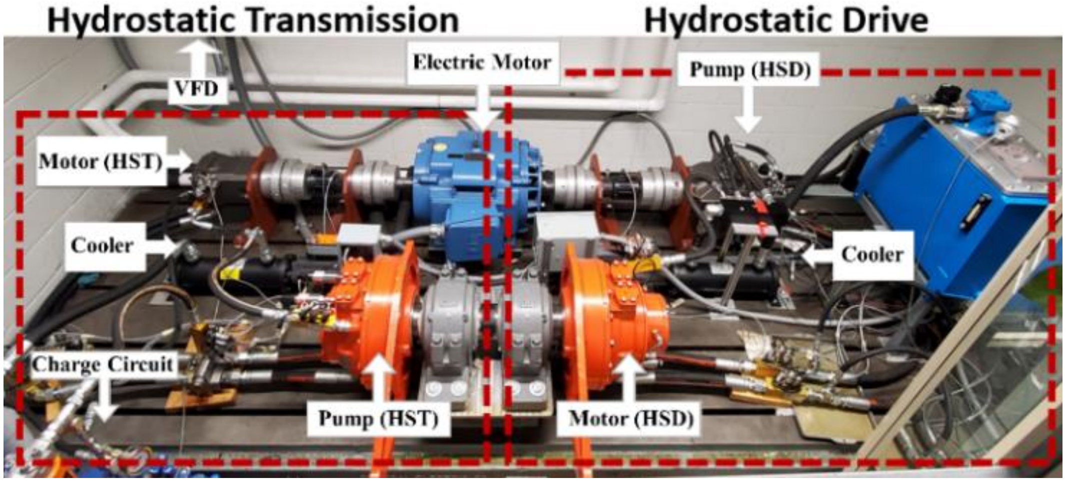

Figure 26. HST test stand at the University of Minnesota – Twin Cities

Mohanty and Stelson [13] modeled the power regenerative dynamometer as a multiple-input multiple-output (MIMO) system with four states: high speed shaft angular speed ω_s, rotor shaft angular speed ω_r, HSD pressure p_d and HST pressure p_t. Control inputs are variable displacements of the drive pump and transmission motor. The VFD control bandwidth is much larger than that of the HSD or HST making the high-speed shaft angular speed variation negligible because of the electrical inertia of the grid. The three remaining dynamic equations are:

$$\dot{p}_d = \frac{\beta_e}{V}\left[\chi D_{pd}\omega_s - D_{md}\omega_r - L_{ld}p_d\right] \tag{6.1}$$

$$J_{test}\dot{\omega}_r + b_r\omega_r = D_{md}p_d - D_p p_t \tag{6.2}$$

$$\dot{p}_t = \frac{\beta_e}{V}\left[D_p\omega_r - \alpha D_m\omega_s - L_{lt}p_t\right] \tag{6.3}$$

The test stand rotor has inertia J_{test} which is much smaller than the wind turbine rotor inertia J_r, which has a significant effect on how the wind turbine responds to changing wind conditions. It is not feasible to install a large flywheel, so real-time simulation is included in the HSD reference command to digitally compensate for the large wind turbine rotor inertia. This is implemented differently when testing HST wind turbine pressure-regulation or HST wind turbine rotor speed-regulation. Swashplate positions χ and α are driven by control input voltages v_d and v_t as given in Equations 6.4 and 6.5.

$$\alpha(s) = \frac{K_t}{\tau_t s + 1}v_t(s) \tag{6.4}$$

$$\chi(s) = \frac{K_d}{\tau_d s + 1}\, v_d(s) \tag{6.5}$$

6.2 Test Stand Control

The outputs are the HSD pressure, rotor speed and HST pressure. The test stand dynamics are described by the transfer function matrix in Equation 6.6.

$$\begin{bmatrix} p_d \\ \omega_r \\ p_t \end{bmatrix} = \begin{bmatrix} g_{11}(s) & g_{12}(s) \\ g_{21}(s) & g_{22}(s) \\ g_{31}(s) & g_{32}(s) \end{bmatrix} \begin{bmatrix} v_d \\ v_t \end{bmatrix} \tag{6.6}$$

The objective is to control the HSD and HST independently as two SISO systems. The relative gain array (RGA) was used in [13] to compare cross-coupling in multiple input-output pairings and select the best control structure of the two resulting SISO systems. The three possible input-output pairings are given in Equation 6.7.

$$\begin{bmatrix} p_d \\ p_t \end{bmatrix} = [G_1(s)] \begin{bmatrix} v_d \\ v_t \end{bmatrix}, \qquad \begin{bmatrix} p_d \\ \omega_r \end{bmatrix} = [G_2(s)] \begin{bmatrix} v_d \\ v_t \end{bmatrix}, \qquad \begin{bmatrix} \omega_r \\ p_t \end{bmatrix} = [G_3(s)] \begin{bmatrix} v_d \\ v_t \end{bmatrix} \tag{6.7}$$

In $G_1(s)$, the HSD and HST pressures are highly coupled so independent control of the two would be very difficult. In $G_2(s)$, HSD pressure is controlled by HSD swashplate and rotor speed is controlled by HST swashplate. In $G_3(s)$, rotor speed is controlled by the HSD swashplate and the HST pressure is controlled by the HST swashplate.

Test stand control is different for conducting experiments on the pressure- and rotor speed-regulated systems because causality changes in the test stand MIMO system. HST and HSD pressure are highly coupled so they cannot be independently controlled. The HSD control output is different whether the HST control output is HST pressure or rotor speed. The objective is to design separate test stand control setups that emulate the same wind effects on the rotor by commanding different control outputs with the HSD. So, test stand control is designed with G_3 for pressure-regulation experiments and G_2 rotor speed-regulation experiments.

Mohanty and Stelson designed a test stand control setup for G_3 to test HST wind turbine pressure-regulation in [13] referred to as test stand control setup 3. The HST pressure control loop tracks a reference pressure calculated using the $K\omega^2$ law. The HSD rotor speed control loop tracks a reference rotor speed that is calculated to emulate the wind turbine rotor dynamics in Equation 6.8 with wind speed u_W.

$$J_r \dot{\omega}_r = \tau_{aero} - \tau_{HST} \tag{6.8}$$

where J_r is the wind turbine rotor inertia, τ_{aero} is the aerodynamic torque and τ_{HST} is the HST reaction torque. τ_{aero} is calculated in real-time by a look-up table using wind speed and rotor speed information. τ_{HST} is calculated in real time as $D_p p_t$. The reference rotor speed is calculated in real-time simulation as

$$\omega_{rref} = \int \frac{1}{J_r} (\tau_{aero} - \tau_{HST}) dt \tag{6.9}$$

The test stand control setup 3 is shown in Figure 27.

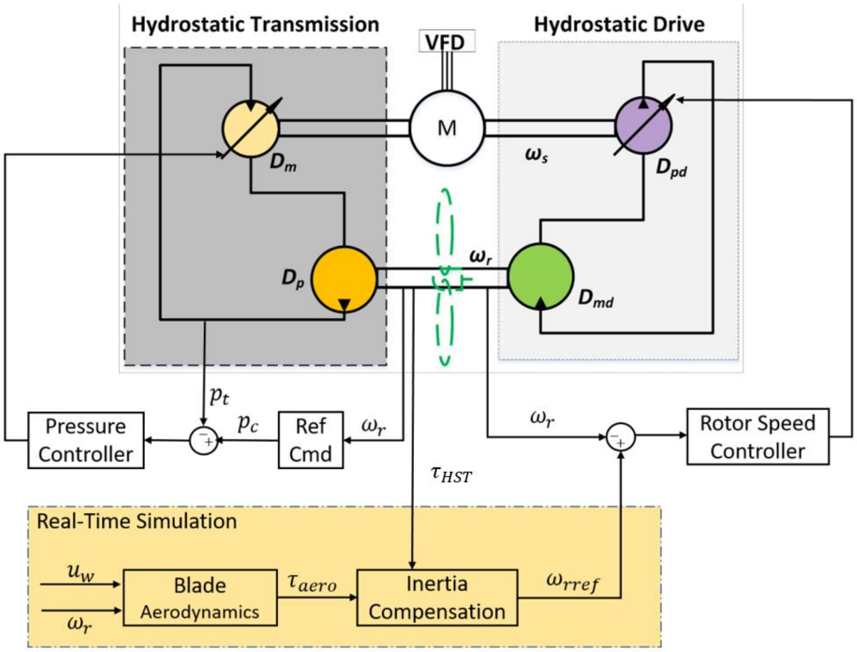

Figure 27. Test stand control setup 3

The methodology in [13] is used in the current study to design a new test stand control scheme for G_2 to test HST wind turbine rotor speed-regulation. This will be referred at as test stand control setup 2. The HST rotor speed control loop tracks a reference rotor speed calculated using the Inverse $K\omega^2$ law. The HSD pressure control loop tracks a reference drive pressure that is calculated to emulate the rigid turbine rotor dynamics in (6.8) under the prescribed wind conditions u_W. A difference here is that HSD pressure is proportional to τ_{HSD} not which is not equal to τ_{HST} due to losses in the test stand rotor shaft.

$$\tau_{HSD} = \tau_{HST} + b\omega_r \tag{6.10}$$

where b is rotational damping and found empirically as $b = \frac{D_{md}p_d - D_p p_t}{\omega_r}$ where $D_{md} = D_p$ in this study. τ_{aero} is calculated as in test stand control setup 3, and $\dot{\omega}_r$ is approximated using a Tustin discrete filtered derivative of the rotor speed measurement. The reference HSD pressure is calculated as

$$p_{dref} = \frac{1}{D_{md}}\left[\tau_{aero}(u_W, \omega_r) - J_r\dot{\omega}_r + b\omega_r\right] \tag{6.11}$$

The test stand control setup 3 is shown in Figure 28.

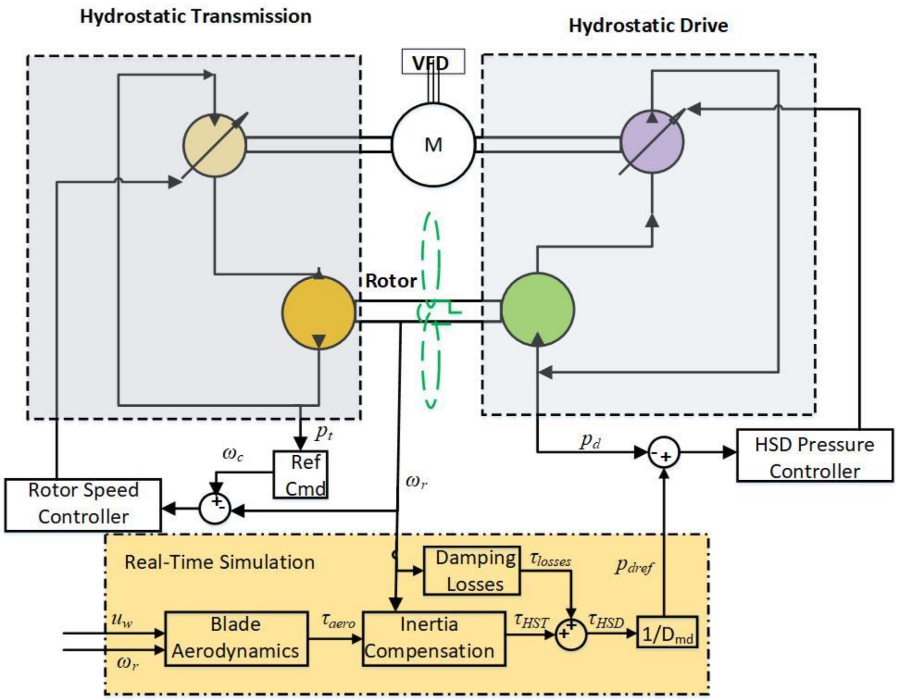

Figure 28. Test stand control setup 2

6.2.1 Decoupling HSD and HST Control Loops

The HSD and HST are coupled, making it difficult to control them independently. A decoupling controller is implemented with a pre-compensator matrix $P_2(s)$ to statically decouple the two control loops. The new MIMO plant $G_2(s)P_2(s)$ is diagonal such that the inputs only influence their intended outputs. So, the rotor speed is only controlled by the HST swashplate input, and the HSD pressure is only controlled by the HSD swashplate input. This static decoupling only decouples the SISO systems in the operating bandwidth. Dynamic decoupling could couple higher frequency dynamics but is sensitive to model uncertainty. The pre-compensator matrix is calculated using the static gain of $G_2(s)$, $G_{2,dc}$.

$$P_2(s) = G_{2,dc}^{-1} diag\left(G_{2,dc}\right) = \begin{bmatrix} 0.6229 & 0.4056 \\ -0.5792 & 0.6229 \end{bmatrix} \tag{6.12}$$

The resulting diagonal plant is

$$G_2(s)P_2(s) = \begin{bmatrix} 288.0473 & 0 \\ 0 & 3.7314 \end{bmatrix} \tag{6.13}$$

The outputs are statically decoupled from their off-diagonal inputs. This creates two statically decoupled SISO control loops for the HST and HSD.

6.2.2 Designing Test Stand SISO Control Loops

In test stand control setup 3, the HSD pressure is controlled by the HSD swashplate actuation voltage v_d. The transfer function from v_d to p_d is:

$$g_{11}(s) = \frac{9920(s^2+4.944s+11.11)}{(s+7.233)(s+2.632)(s^2+5.863s+20.1)} \tag{6.14}$$

A PID controller $C_1(s) = 0.0027 + \frac{0.0072}{s} + \frac{0.0002s}{0.0256s+1}$ was designed in [18] to control p_d with zero tracking error and disturbance rejection at low frequencies with a bandwidth of 2 rad/s. The HST rotor speed is controlled by the HST swashplate actuation voltage v_t. The transfer function from v_t to ω_r is:

$$g_{22}(s) = \frac{221.78(s+8.152)}{(s+7.233)(s+3.333)(s^2+5.863s+20.1)} \tag{6.15}$$

Ideally, the HST rotor speed control loop from simulation would be accurately emulated by the test stand. However, practical challenges with differentiation and computational delay with the inertial compensation in test stand control setup 2 limit the test stand HST rotor speed control loop bandwidth to 1.5 rad/s. So, a PID controller $C_2(s) = 0.03805 + \frac{0.1903}{s} + \frac{0.003805s}{0.0256s+1}$ is designed to control ω_r with zero tracking error and disturbance rejection at low frequencies with a bandwidth of 1 rad/s. For a fair comparison, the PID controller for HST pressure control in test stand control setup 3 is modified as $C_3(s) = 0.0011132 + \frac{0.0056}{s} + \frac{0.00011132}{0.0256s+1}$ to also have a bandwidth of 1 rad/s. Figure 29 shows closed-loop frequency response of the HST pressure and rotor speed control loops.

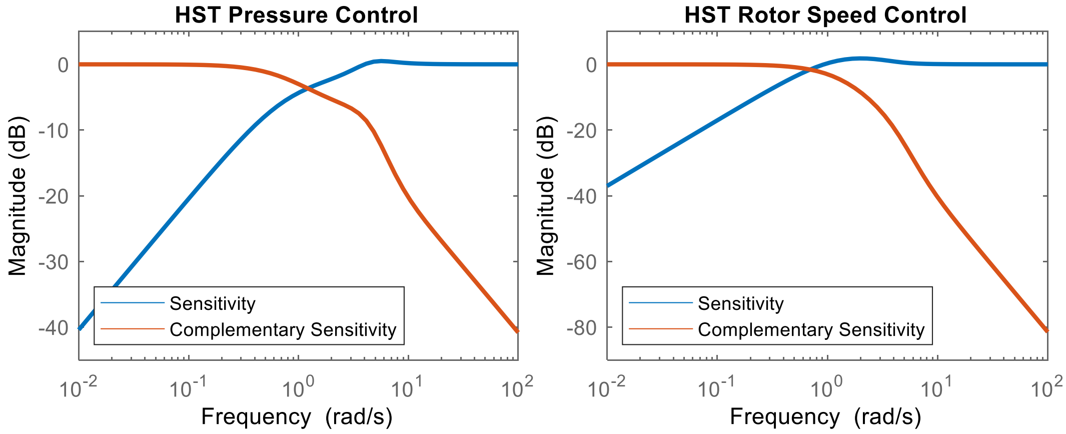

Figure 29. Frequency response of closed-loop HST pressure (left) and HST rotor speed (right) control

The HST pressure control loop in test stand control setup 3 and HST rotor speed control loop in test stand control setup 2 are designed to have comparable frequency responses in the operating bandwidth, and their responses deviate around 2 rad/s. External wind inputs are filtered to reduce excitation of higher frequencies. The two plants have identical poles but different zeros, causing their high frequency responses to roll off at different rates. The

HST pressure control loop in test stand control setup 3 attenuates slower than the HST rotor speed control loop in test stand control setup 2.

Gain and phase margin of the open-loop system determine the relative stability of the closed-loop system. The gain margin G_M is how much the open-loop gain at -180 degrees of phase shift needs to increase to make the closed-loop system unstable. The phase margin Φ_{m} is how much the open-loop phase lag at unity gain needs to increase to make the closed-loop system unstable. The HST pressure and rotor speed control loop gains are shown in Figure 30.

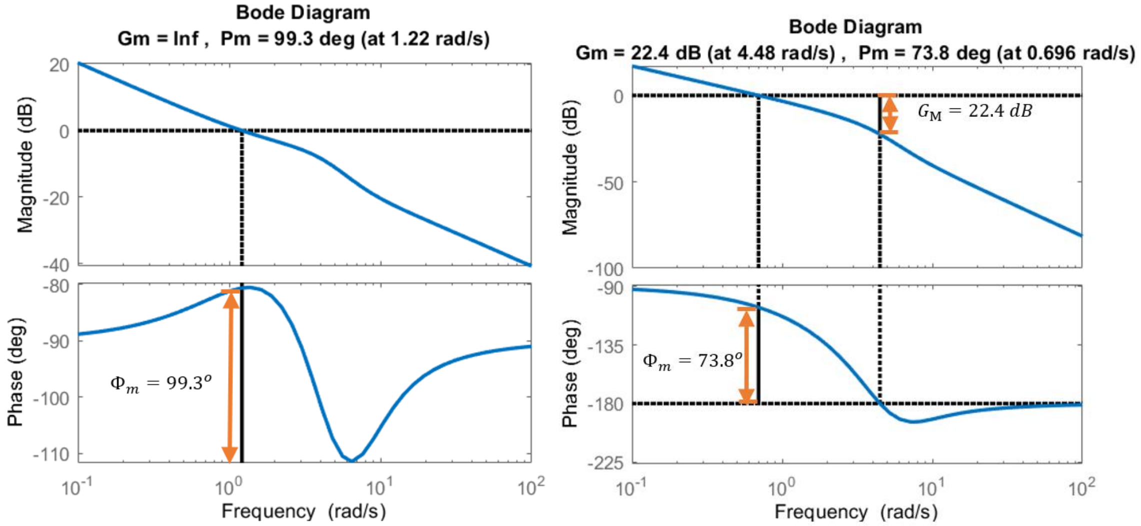

Figure 30. HST pressure (left) control loop gain and rotor speed control loop gain (right)

The HST pressure control loop gain has $G_M = \infty$ and $\Phi_M = 99.3^o$. The HST rotor speed control loop has $G_M = 22.4\ dB$ and $\Phi_M = 73.8^o$. The HST pressure control loop has a larger gain margin so it is expected to be more robust to unmodeled conditions than the rotor speed-regulated system. The HST pressure control loop also has larger phase margin so it is expected to be more robust to time delays than the HST rotor speed control loop.

6.3 Experiment Results and Discussion

This section presents an experimental comparison of the HST wind turbine pressure- and rotor speed-regulated systems. System transient behavior under stepped wind conditions, steady wind for varied control law gain K, and turbulent wind conditions are studied. States, power, and time are dimensionless, with scaling factors selected for 6 m/s wind. See Appendix 1. All times such as settling time and delay are in dimensionless time units.

6.3.1 Stepped Wind Study

Transient behavior of the experimental pressure- and rotor speed-regulated systems is tested under stepped wind conditions. Both systems are initialized for $u_W = 6\ m/s$. The wind input is filtered to reduce excitation of higher frequencies.

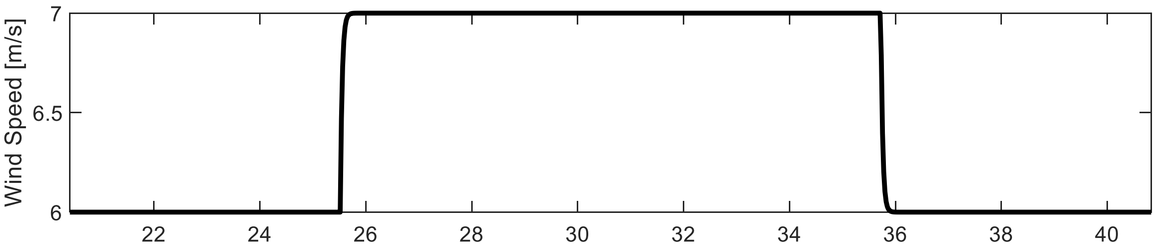

Figure 31. Stepped wind profile

The dimensionless reference, output and control law error responses of the pressure- and rotor speed-regulated systems are shown in Figures 32 and 33. Output responses from simulated systems with comparable control bandwidth are included for comparison.

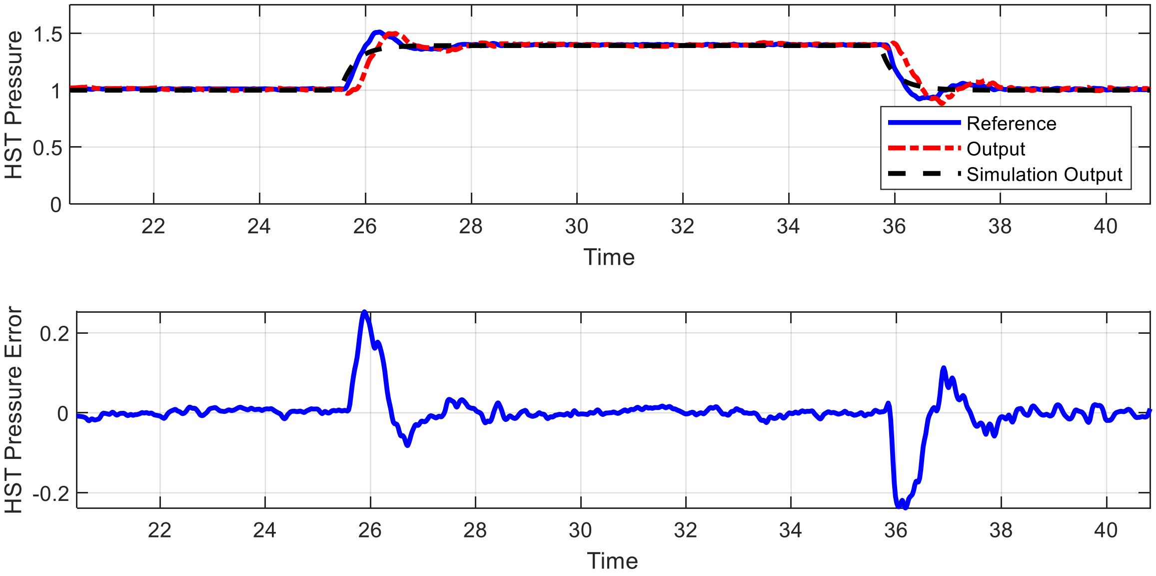

Figure 32. Reference, output and error responses of pressure-regulated system under stepped wind

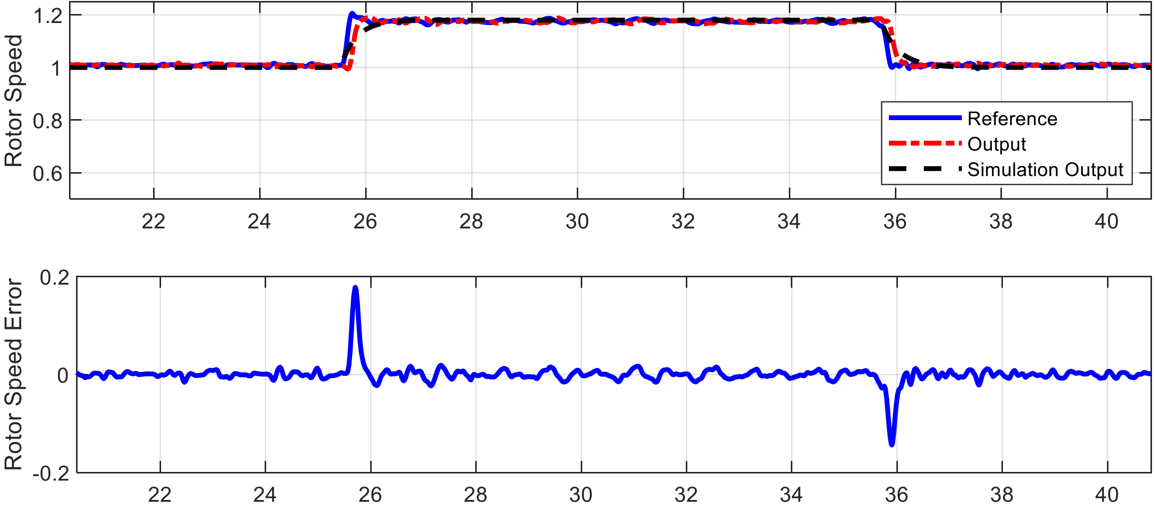

Figure 33. Reference, output and error responses of rotor speed-regulated system under stepped wind

The dimensionless state and power response of the pressure- and rotor speed-regulated systems are compared in Figure 34.

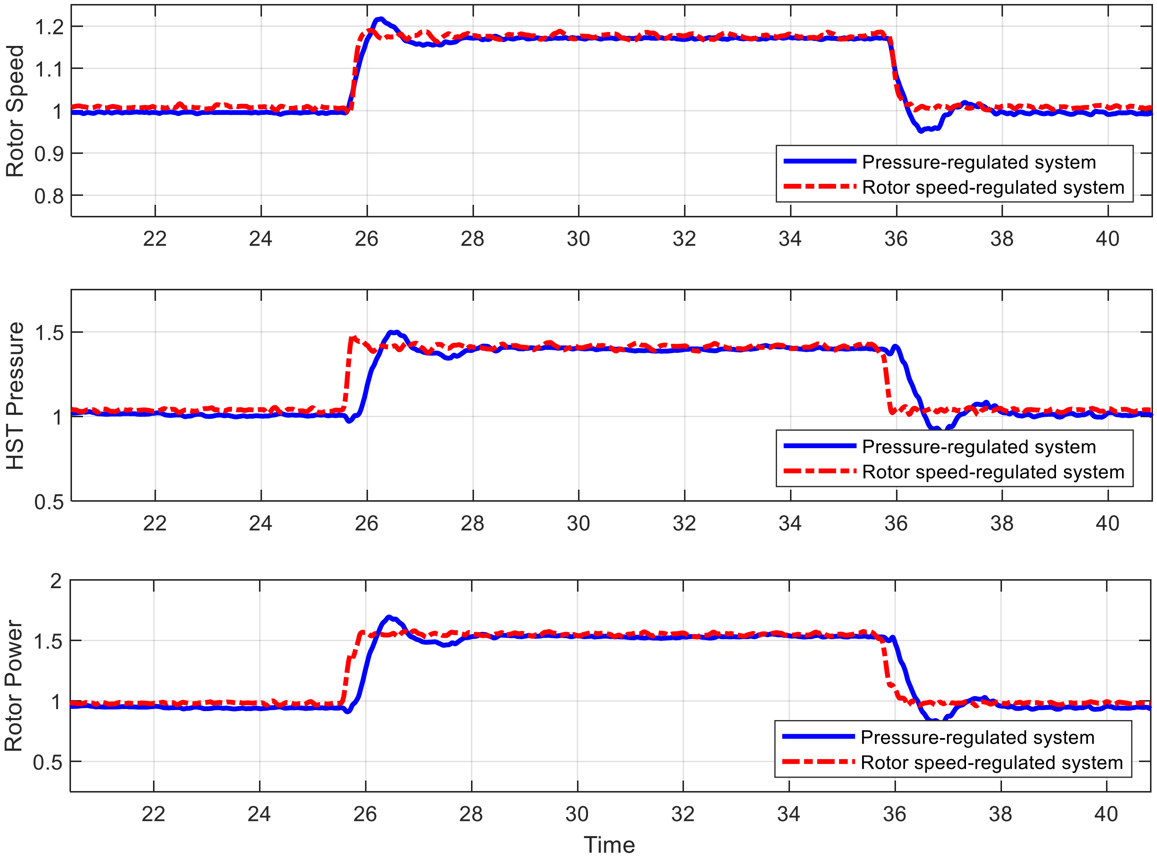

Figure 34. Dimensionless state and power responses under stepped wind

The pressure- and rotor speed-regulated systems both track their references at steady-state but differ in their transient behavior. The HST pressure-regulated system output response has 25.13% overshoot and 0.2 of delay which slows its ability to track its reference, settling in 2.26. There is no delay or overshoot in the simulated output response which settles in 0.93. Note that the reference follows a similar path to the simulated output until the overshoot, which shows that the delay is a driving factor in the discrepancy between the experimental and simulation results. The delay is likely due in part to the test stand's interaction with the real-time simulation and inertial compensation. The HST rotor speed-regulated system output response has 7.34% overshoot and 0.13 of delay which is relatively minor and does not hinder its ability to track its reference, settling in 0.64. There is no delay or overshoot in the corresponding simulated output response which settles in 1.05.

The pressure- and rotor speed-regulated systems experience different time delays where time delay in the pressure-regulated system is nearly twice that of the rotor speed-regulated system. So, even though the HST pressure control loop is expected to be more robust to time delays than the HST rotor speed control loop, the larger time delay in the pressure-regulated system has a larger effect on stability than the smaller time delay in the rotor speed-regulated system.

Differences between the experimental and simulated output responses are likely due to unmodeled dynamics in the test stand. Unmodeled delay is present in both experimental systems' output responses. Delay in rotor speed and pressure affects both control loop references which may contribute to the difference between experiments and simulation. Unmodeled HSD dynamics are also present in the test stand. The HSD and HST control loops are only statically decoupled, so their dynamics with changing wind conditions are coupled. These coupled HSD dynamics are not present in the simulation model and would not be present in the real HST wind turbine. This is a limitation of the test stand. Despite these differences, the experimental systems respond comparably to their corresponding simulated models.

6.3.2 Power capture study

The next step is to investigate the effect of varying K on power capture of the pressure- and rotor speed-regulated systems under steady wind conditions. The $C_p\ vs.\lambda$ curve has a peak of $C_{p.max} = 0.41$ at optimal tip-speed ratio $\lambda_* = 6.5$. An ideal controller for this

$C_p\ vs.\lambda$ curve has a control law gain $K = K_{ideal}$. Using $K \neq K_{ideal}$ represents when the controller is not optimized for the true $C_p\ vs.\lambda$ curve. Figure 35 shows variations in K affect dimensionless rotor power when both systems operate under constant 6 m/s wind.

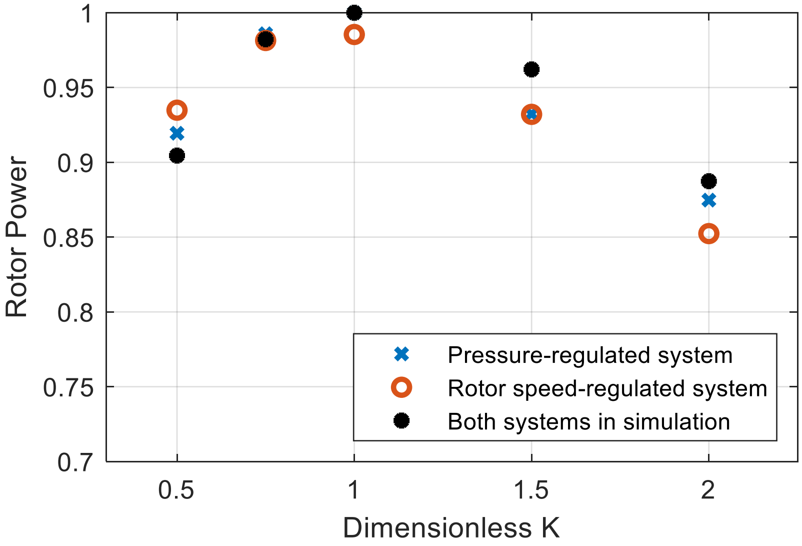

Figure 35. Power capture as a function of control law gain

As expected, using $K \neq K_{ideal}$ results in less power capture than when $K = K_{ideal}$. Both control approaches experience reduced power for $K \neq K_{ideal}$ with power losses increasing as K moves farther away from its ideal value. Practical experimental factors result in slightly different steady-state power capture between the two systems. The rotor speed-regulated system captures 1.45% less power than the pressure-regulated system for the ideal control law gain, but the rotor-speed regulated system captures between 2.56% less and 0.41% more power than the pressure-regulated system for other conditions. This does not account for differences during transients.

6.3.3 Turbulent Wind Study

The next step is to investigate the tracking and power capture of the systems under turbulent wind conditions. A small constant $C = -0.0182$ is added to wind data collected from the

Eolos research wind turbine in Rosemount, MN to get a turbulent wind profile with mean wind speed of $\bar{u}_W = 6\,m/s$ [26]. The dimensionless state and power responses of the pressure- and rotor speed-regulated systems under turbulent wind with $\bar{u}_W = 6$ are compared in Figure 36.

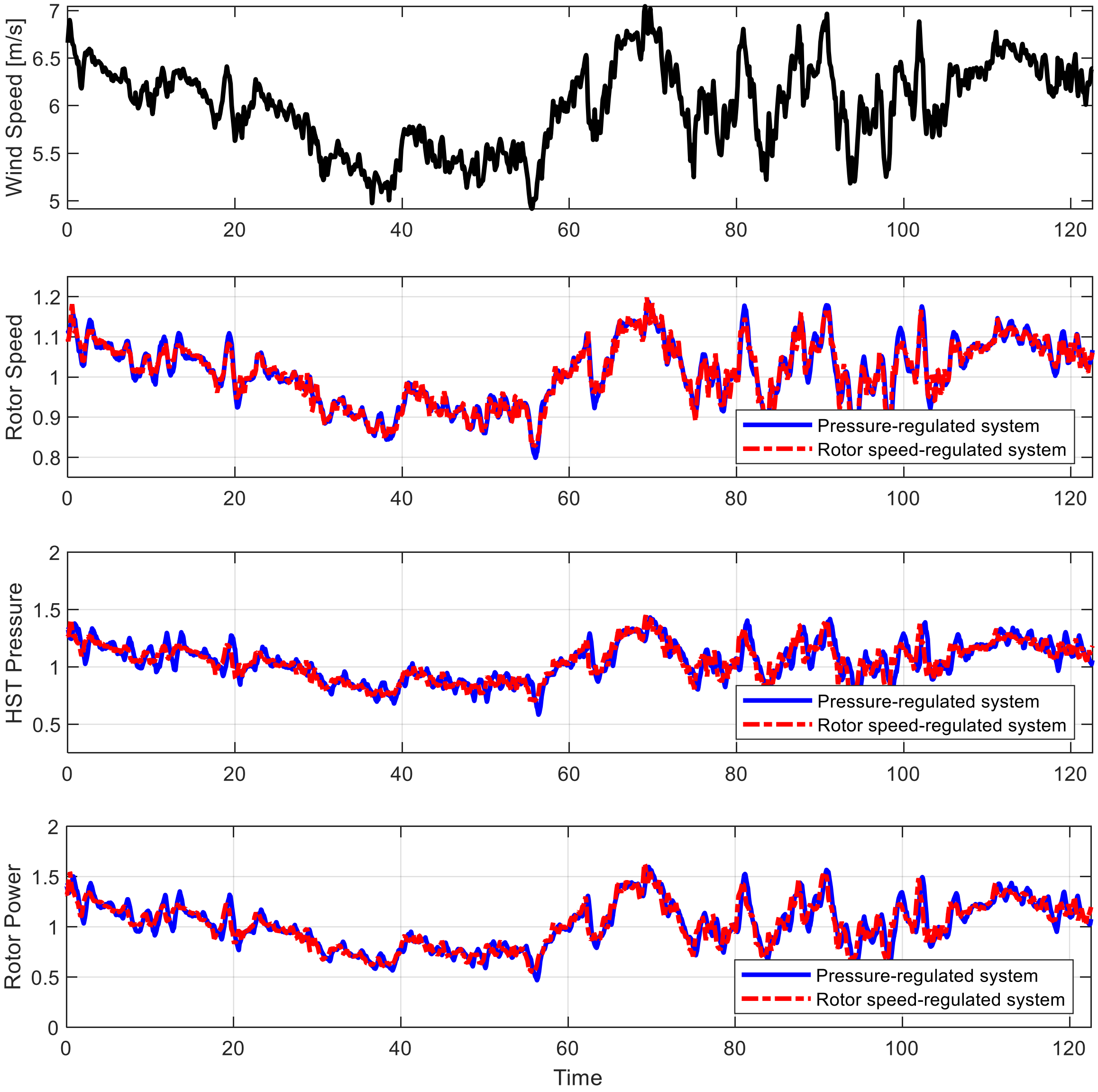

Figure 36. Dimensionless state and power responses under turbulent wind with mean wind speed v=6 m/s

The pressure-regulated system captures an average dimensionless power of 1.0235. The rotor speed-regulated system captures an average dimensionless power of 1.0203.

Operating under turbulent wind captures more power than steady wind with the same mean speed because wind power is proportional to the cube of the wind speed, so more power is gained above the mean speed than power is lost below the mean speed. The difference in average power capture between the two systems is less than 1%.

6.4 Conclusions from the Experimental Study

This study investigates the performance of pressure- and rotor speed-regulated HST wind turbines using on the power regenerative hydrostatic test stand at the University of Minnesota. The test stand consists of a hydrostatic drive coupled with a hydrostatic transmission via common generator and rotor speed shafts.

Test stand control is different for conducting experiments on the pressure- and rotor speed-regulated systems because causality changes in the test stand MIMO system. The HST and HSD control outputs cannot be the same since this would violate causality,, so the HSD control output is different from the HST control output depending on whether HST output is pressure or rotor speed. Further, two separate test stand control setups are designed to emulate the same wind effects on the rotor by commanding different HSD control outputs. The test stand control setup for conducting experiments on the HST pressure-regulated system was developed in [13]. A new test stand control setup for conducting experiments on the HST rotor speed-regulated system is designed in this study using the same methodology. The test stand controllers differ from simulation because the test stand has practical limitations which limit the test stand controllers' bandwidth.

Experiments are conducted to validate conclusions from the analysis and simulation. The first study shows that the pressure- and rotor speed-regulated HST wind turbines both experience delays and differ in their transient response to a stepped wind profile. The second study shows that the pressure-regulated system captures 1.44% more power than the rotor speed-regulated system when $K = K_{ideal}$ but the two have comparable power losses when $K \neq K_{ideal}$. The third study shows that the pressure- and rotor speed-regulated HST wind turbines capture comparable power under turbulent wind conditions.

7 Chapter 7: Conclusions and Future Work

7.1 Conclusions

The $K\omega^2$ law is implemented in HST wind turbines using pressure-regulation control as $p_c=K'\omega^2$ or rotor speed-regulation control as $\omega_c=(p/K')^{1/2}$. These two control approaches are investigated using linear root locus analysis and nonlinear numerical simulation. Root locus analysis shows that systems using P- and PI-control have poorly damped responses because they have poles with large imaginary components regardless of the loop gain. Systems using PID-control avoid this issue by drawing the complex poles closer to the negative real axis. Root locus analysis also shows that both systems are fundamentally limited in speed of response, because of a slow dominant pole.

Simulation studies show that the two nonlinear systems respond nearly identically to unsteady operating conditions and variations in a and K. Experiments of the two control approaches were conducted on the power regenerative hydrostatic test stand at the University of Minnesota. The pressure- and rotor speed-regulated systems perform comparably under steady and turbulent wind and tested values of K. However, the pressure regulated system is more robust to unmodeled conditions because it has higher gain and phase margin than the rotor speed-regulated system.

Gain margin and phase margin analysis show that pressure-regulation is more robust than rotor speed-regulation for $K\omega^2$ control in region 2. This study also offers insight into hydrostatic wind turbine dynamics. Insight into the relative dynamics of the two control approaches, magnitude of damping and leakage effects, conditions for stability using classical controller designs and fundamental limitations on system response were found using a novel root-locus approach where poles and zeros were both functions of loop gain because the system equations are not in Evan's form.

7.2 Future Work

7.2.1 Improvements to current study

The linear analysis in this study is shown to be valid over a wide range of operation. This range of operation could be extended with nonlinear analysis tools. For example, Lyapunov's Direct Method (LDM) is a powerful tool to describe the stability of the full nonlinear dynamical equations. Identifying a scalar positive-definite Lyapunov function candidate $V(x)$ whose time derivative $\dot{V}(x)$ is non-positive would make a strong analytical case for stability in the proposed nonlinear pressure- and rotor speed-regulated HST wind turbine systems [25].

The parabolic model for the power characteristic is also shown to be valid over a wide range of operation. Modeling the dimensionless power characteristic as a higher-order function of rotor speed could better represent the shape of the true dimensionless power curve far away from the peak. The dimensionless power curve is also asymmetrical, so a piece-wise function may be a better approximation.

The effect of delay is discussed for experiments in the current study but could be extended to simulation. Introducing delay into the simulation model would show much delay each system can take before destabilizing. This would support the current conclusions on robustness.

7.2.2 Dynamically estimate rotor torque for MPPT control

Implementing the $K\omega^2$ law as pressure-regulation in HST wind turbines uses a proportional relationship between transmission pressure and rotor torque. Unmodeled dynamics can cause suboptimal power capture. It is advantageous to measure rotor torque directly, but large torque transducers are expensive. Dynamic estimation may be a cheaper solution to get more accurate rotor torque measurements.

An unknown-input observer (UIO) is similar to a full state observer but treats the disturbance differently. The UIO incorporates the disturbance into an augmented state vector and estimate it using Luenberger observer [21]. For an HST, the aerodynamic torque $\hat{T}$ can be included in the augmented state vector and estimated in real-time. The estimator dynamics are shown in Equation 7.1.

$$\begin{bmatrix} \dot{\hat{\omega}} \\ \dot{\hat{p}} \\ \dot{\hat{\alpha}} \\ \dot{\hat{T}} \end{bmatrix} = \begin{bmatrix} -\frac{b_r}{J} & -\frac{D_p}{2\pi J} & 0 & \frac{1}{J} \\ \frac{\beta_e D_p}{2\pi V} & -\frac{\beta_e L}{V} & -\frac{\beta_e D_m \omega_s}{2\pi V} & 0 \\ 0 & 0 & -\frac{1}{\tau_{sp}} & 0 \\ 0 & 0 & 0 & 0 \end{bmatrix} \begin{bmatrix} \hat{\omega}_r \\ \hat{p} \\ \hat{\alpha} \\ \hat{T} \end{bmatrix} + \begin{bmatrix} 0 \\ 0 \\ \frac{1}{\tau_{sp}} \\ 0 \end{bmatrix} [\alpha_{cmd}] \tag{7.1}$$

The rotor torque dynamics are modeled as constant because the effective wind conditions are slow-moving relative to the observer dynamics. Implementing an UIO to estimate rotor torque only requires software changes so it is a cost-effective alternative that has potential to produce better MPPT than the current pressure approximation. Implementing an UIO would also generate filtered estimates for rotor speed and pressure which could improve the current limitation with test stand control for test stand control setup 2 in Chapter 6.

7.2.3 Dynamically estimate wind speed and Model Predictive Control (MPC)

The idea above can be extended to estimate wind speed. Wind speed information is directly linked to the C_p vs λ curve and could be useful for MPPT control. While Light Detection And Ranging (LiDAR) is becoming more affordable, wind measurement at one location does not give a complete picture of the wind interacting with the wind turbine because wind varies spatially and temporally [28]. However, LiDAR measurement could be joined with a physics-based model to get a more confident estimation of the effective wind speed on the rotor.

Wind speed estimation could also be useful with Model Predictive Control (MPC) [29] in anticipating wind conditions before they reach the rotor. Future wind information estimated from LiDAR measurements upwind of the wind turbine would allow the wind turbine controller to predict the wind speed change in advance and command the system accordingly.

Bibliography

[1] U.S. Energy Information Administration, “EIA projects that renewable generation will supply 44% of U.S. electricity by 2050,” 2023.

[2] R. Wiser *et al.*, “Wind Vision: A New Era for Wind Power in the United States,” *Electr. J.*, vol. 28, no. 9, pp. 120–132, 2015.

[3] Office of Energy Efficiency and Renewable Energy, “Utility-Scale Wind Energy,” 2023. https://windexchange.energy.gov/markets/utility-scale

[4] U.S. Department of Energy, “Wind Vision Report by United States Department of Energy,” 2008. https://www.energy.gov/eere/wind/wind-vision

[5] A. Orrell, K. Kazimierczuk, and L. Sheridan, “Distributed Wind Market Report: 2021 Edition,” 2021.

[6] A. C. Orrell, N. A. F. Foster, J. S. Homer, S. L. Morris, D. Preziuso, and E. Poehlman. 2017 distributed wind market report. Technical report, Pacific Northwest National Lab.(PNNL), Richland, WA (United States), 2018.

[7] IRENA. “Renewable energy technologies: Cost analysis series wind turbine,” Journal of solar energy engineering, 1(5/5), 2012.

[8] W. Chen, X. Wang, F. Zhang, H. Liu, and Y. Lin, “Review of the Application of Hydraulic Technology in Wind Turbine,” *Wind Energy*, Vol. 23, 2020, pp. 1495-1522.

[9] P. J. Chapple, M. Niss, K. E. Thomsen, “Wind Turbines with Variable Hydraulic Transmission, and Electrically Excited synchronous Generators Directly Connected to the Grid,” *Proceedings of the ASME/Bath Symposium on Fluid Power and Motion*

Control, Sept. 12-14, 2012, Bath, UK.

[10] W. Rampen, D. Dumnov, J. Taylor, H. Dodson, J. Hutcheson, and N. Caldwell, “A Digital Displacement Hydrostatic Wind-Turbine Transmission,” *International Journal of Fluid Power*, Vol. 22, no. 1, 2021, pp. 87-112.

[11] P. Dvorak, “Hello Sea Angel: Hydraulic Drive Train Could Provide 7MW Offshore Turbine,” *Wind Power Engineering and Development*, Jan 25, 2013.

[12] J. Schmitz, M. Vukovic and H. Murrenhoff, “Hydrostatic Transmission for Wind Turbines – An Old Concept, New Dynamics,” *Proceedings of the ASME/Bath Symposium on Fluid Power and Motion Control*, Oct 6-9, 2013, Sarasota, FL, USA.

[13] B. Mohanty and K. A. Stelson, “Dynamics and Control of an Energy-Efficient, Power-Regenerative, Hydrostatic Wind Turbine Dynamometer,” *Energies , vol. 15*, 2022.

[14] E. B. Mohr, B. Mohanty, and K. A. Stelson, “Short-Term Energy Storage System for Hydraulic Hybrid Wind Turbine Transmission,” Proc. 2020 Bath/ASME Symp. Fluid Power Motion Control, 2020.

[15] K. E. Johnson, L. Y. Pao, M. J. Balas, and J. F. Lee, “Control of Variable-Speed Wind Turbines: Standard and Adaptive Techniques for Maximizing Energy Capture,” *IEEE Control Syst*., vol. 26, no. 3, pp. 70–81, 2006.

[16] W. Leithead, “Variable Speed Operation – Does it Have Any Advantages?,” *Wind Engineering*, vol. 13, no. 6, pp. 302-314, 1989.

[17] W.E. Leithead, “Control Systems for Wind Turbines,” *Wind Engineering*, vol. 13, no. 6, pp. 293-301, 1989.

[18] B. Mohanty and K.A. Stelson, “High Fidelity Dynamic Modeling and Control of

Power Regenerative Hydrostatic Wind Turbine Test Platform," in *Proceedings of the 2018 ASME/Bath Symposium on Fluid Power and Motion Control*, Bath, UK. September 12–14, 2018.

[19] D. Escobar-Naranjo, B. Mohanty, and K. A. Stelson, "Using Extremum Seeking Control to Improve the Power Capture of Midsize Hydrostatic Wind Turbines," in *Proceedings of the 2021 ASME/Bath Symposium on Fluid Power and Motion Control*, Virtual, Online. October 19–21, 2021.

[20] P. Chapple and M. Niss, "A Wind Turbine with Hydrostatic Transmission and LVRT Control," European patent EP2481917A1, Aug. 1, 2012.

[21] L. Y. Pao and K. E. Johnson, "A Tutorial on the Dynamics and Control of Wind Turbines and Wind Farms," In *Proceedings of the 2009 IEEE American Control Conference*, St. Louis, MO, USA, 2009, pp. 2076-2089.

[22] B. Mohanty, S. Dhople and K.A. Stelson, "A Dynamical Model for a Hydrostatic Wind Turbine Transmission Coupled to the Grid with a Syncrhonous Generator," In *Proceedings of the 2019 American Control Conference*, Philadelphia, PA, USA, 2019, pp. 5774-5779.

[23] Polaris. Polaris America. http://www.polarisamerica.com/.

[24] W. Hahn, "Stability of Motion," *Grundlehren der mathematischen: GL, vol. 138*, 1967.

[25] G.F. Franklin, D. Powell and A. Emami-Naeini, *Feedback Control of Dynamic Systems*, 7th ed. Upper Saddle River, NJ, USA: Pearson, 2014.

[26] Stone, N. EOLOS Educational Data Set: An Overview Available online: http://eolos.umn.edu/sites/eolos.dl.umn.edu/files/general/eolos_educational_data_s

et.pdf (accessed on 17 October 2022).

[27] R.H.C Takahashi, P.L.D. Peres, “Unknown Input Observers for Uncertain Systems: A Unifying Approach,” *European Journal of Control, vol. 5*, 1999.

[28] E. J. Novaes Menezes, A. M. Araújo and N. S. Bouchonneau da Silva, “A review on wind turbine control and its associated methods,” *Journal of Cleaner Production*, vol. 174, pp. 945-953, 2018.

[29] F. Wang and K.A. Stelson, “Model Predictive Control for Power Optimization in a Hydrostatic Wind Turbine,” In *Proceedings of the 13th Scandinavian International Conference of Fluid Power SICFP2013*, Linkoping, Sweden. June 3-5, 2013.

Appendices

Appendix 1: Specifications for a 60 kW Wind turbine

This study investigates the performance of an HST in a 60 kW wind turbine manufactured by Polaris. Table 1 lists specifications for the Polaris P21-60 60 kW wind turbine.

Table 1. Specifications for a Polaris P21-60 60 kW Wind turbine

Specification	Symbol	Test Turbine
Turbine Model		P21-60
Power rating at output shaft	P	60 kW
Number of blades		3
Rotor Radius	R	10.6 m
Hub Height	H	30 m
Rated Wind Speed	u_{wr}	10 m/s
Max Rotational Speed	W_{rmax}	58 RPM
Power coefficient	C_{pmax}	0.41
Optimal TSR	λ_{opt}	6.5
Rotor Inertia	J_t	14100 kgm^3

The Hydrostatic Transmission for this application was designed in [18].

Table 2 lists specifications for the Hydrostatic Transmission.

Table 2. Specifications for a 60kW Hydrostatic Wind turbine

Specification	Symbol	Value
Hydraulic Pump Displacement	D_p	2512 cc/rev
Hydraulic Motor Max Displacement	D_m	135 cc/rev
Effective Bulk Modulus	β_e	6051.5 bar
Leakage in HST	L_t	0.010 lpm/bar
Fluid Line Volume	V	9.82e-4 m^3
Swashplate Time Constant	τ_{sp}	0.39 s

The states and time in the HST wind turbine dynamic model are scaled to equal one at the stationary point. The scaling factors are equal to their values at the stationary point and found by conducting simulations of a 60 kW HST wind turbine operating steadily at the stationary point. Table 3 lists the scaling factors for stationary points in region 2.

Table 3. Scaling factors for various stationary points in region 2

Wind speed	Rotor Speed ω_m [rad/s]	Pressure p_m [Pa]	Swashplate angle, α_m	Torque T_m [Nm]	Power P_m [W]
4 m/s	2.4163	0.5890e7	0.3514	2.3381e3	5.65E+03
5 m/s	3.0285	0.9018e7	0.4469	3.6449e3	1.10E+04
6 m/s	3.6416	1.2498e7	0.5342	5.2410e3	1.91E+04
7 m/s	4.2555	1.7203e7	0.6144	7.1259e3	3.03E+04
8 m/s	4.8689	2.3132e7	0.7037	9.3018e3	4.53E+04

The dimensionless model is includes constants a, c and ψ. a is the curvature of the modeled power characteristic. In this study, a realistic value of a is determined by fitting the modeled power characteristic to true dimensionless power curves for chosen stationary points. The true dimensionless power curves for stationary points at 3, 6 and 9 m/s wind speed are calculated using the $C_p\ vs\ \lambda$ curve in figure (5) and scaled. Remarkably, selecting $a = 2$ results in a good fit over a wide operating range for all three stationary points.

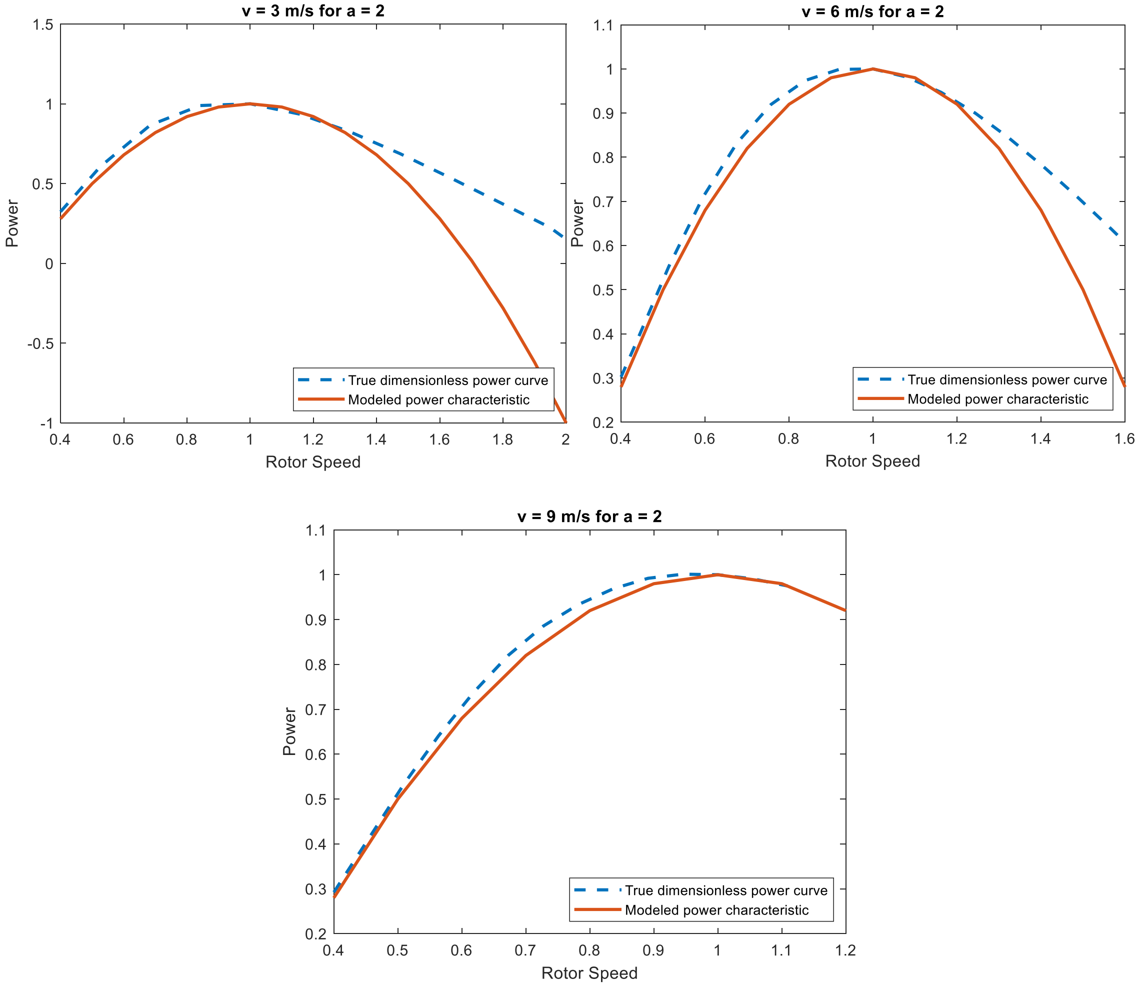

Figure 37. Scaled power curves and fitted power characteristics at v=3,6,9 m/s

For a stationary point at 6 m/s wind speed, this fit is good for a wide range of rotor speeds $\in (0.4,1.2)$. The modeled power characteristic becomes steeper than the dimensionless power curve at rotor speeds higher than 1.2.

c is the dimensionless ratio of hydraulic response time to rotor response time. ψ is the dimensionless ratio of swashplate response time to rotor response time. Both constants differ for each stationary point and are calculated using the scaling factors from table 3. Table 4 lists values of c and ψ for stationary points at 3, 6 and 9 m/s wind speed.

Table 4. Typical values of c and ψ for a 60 kW HST wind turbine

Wind speed, v [m/s]	$c = \frac{D_p}{2\pi}\sqrt{\frac{\beta J}{V T_m K}}$	$\psi = \frac{J\omega_m}{T_m \tau_{sp}}$
3	52.3358	49.4171
6	26.2545	25.1210
9	17.5203	16.8408

Both ratios are much greater than one for all steady operating conditions in Region 2. This means that the mechanical rotor system is significantly slower than the hydraulic and actuator systems and likely limits the system speed of response.

The dimensionless model neglects rotor damping b and leakage L losses. Both constants differ for each stationary point and are calculated using the scaling factors from table 3.

Table 5 lists dimensional values of b and L for a 60 kW HST wind turbine.

Table 5. Typical parameter values for a 60 kW HST wind turbine

Turbine Parameter/Maximum Operating Conditions	Parameter Values
Rotor damping, b	38.9324 $N-m-s$
Leakage, L	1.6667e-12 $\frac{m^3}{s-Pa}$
Control Law Gain, K	384.4405 $\frac{Nms^2}{rad^2}$
Pump displacement, D_p	0.0025 $\frac{m^3}{rev}$

Table 6 lists values of $\hat{b}$ and $\hat{L}$ for stationary points at 3, 6 and 9 m/s wind speed.

Table 6. Typical values of $\hat{b}$ and $\hat{L}$ for a 60 kW HST wind turbine

Wind speed, v [m/s]	T_m	$\hat{b} = \frac{b}{\sqrt{T_m K}}$	$\hat{L} = \frac{4\pi^2 V \sqrt{T_m K}}{\beta D_p^2} L$
3	1.3189e3	0.0547	1.2049e-14
6	5.2410e3	0.0274	2.4018e-14
9	1.1769e4	0.0183	3.5992e-14

Appendix 2: Root Loci Tuning for PI-Controlled Systems

The PI-controlled systems here have two control degrees of freedom, K_p and K_i. $r_i = K_i/K_p$ can be used to shape the loci. Varying r_i instead of K_i preserves the loop gain K_p as r_i varies. Figure 38 shows pole root loci for the pressure-regulated system with various chosen values of r_i.

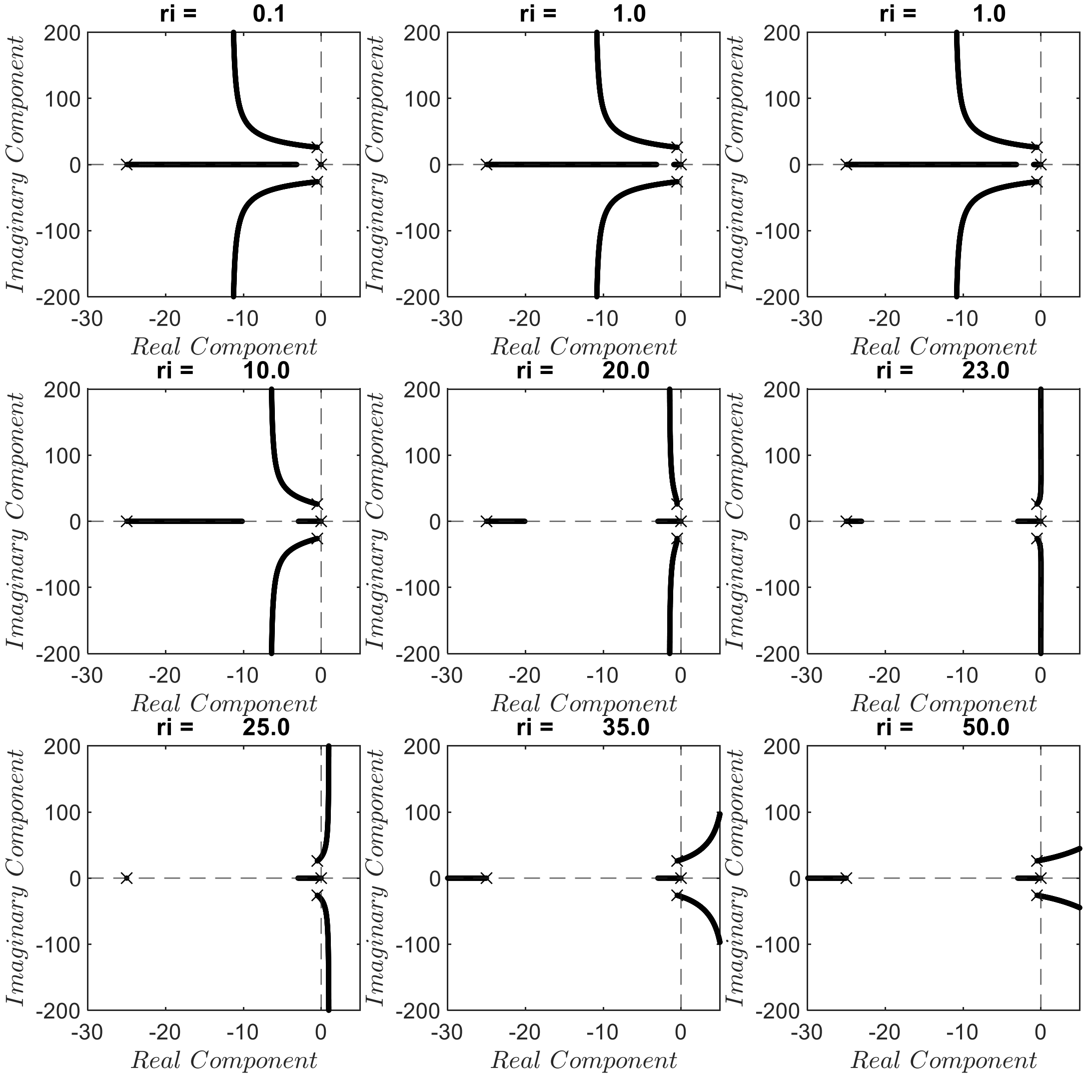

Figure 38. Pole root loci of pressure-regulated system with PI-control for chosen values of r_i

These loci apply for both pressure- and rotor speed-regulated systems because the systems' transfer functions are identical for all r_i if $K_{p,rs} = 2K_{p,pr}$. This means that, even though the closed-loop poles for $K_{p,rs} = K_{p,pr} = x$ are different, the closed-loop poles follow the same branches as $K_{p,rs}$ and $K_{p,pr}$ change. The closed-loop complex branches go into the LHP before moving vertically away from the real axis. Larger values of r_i draw the complex conjugate asymptotes toward the Right Half Plane (RHP) and destabilize the systems when $r_i \geq 23$. The closed-loop real branches asymptotically approach $s = -3$ and $s = -r_i$. Figures 39-41 show rotor speed, pressure and swashplate zero root loci for the pressure-regulated systems with various chosen values of $r_i \leq 23$.

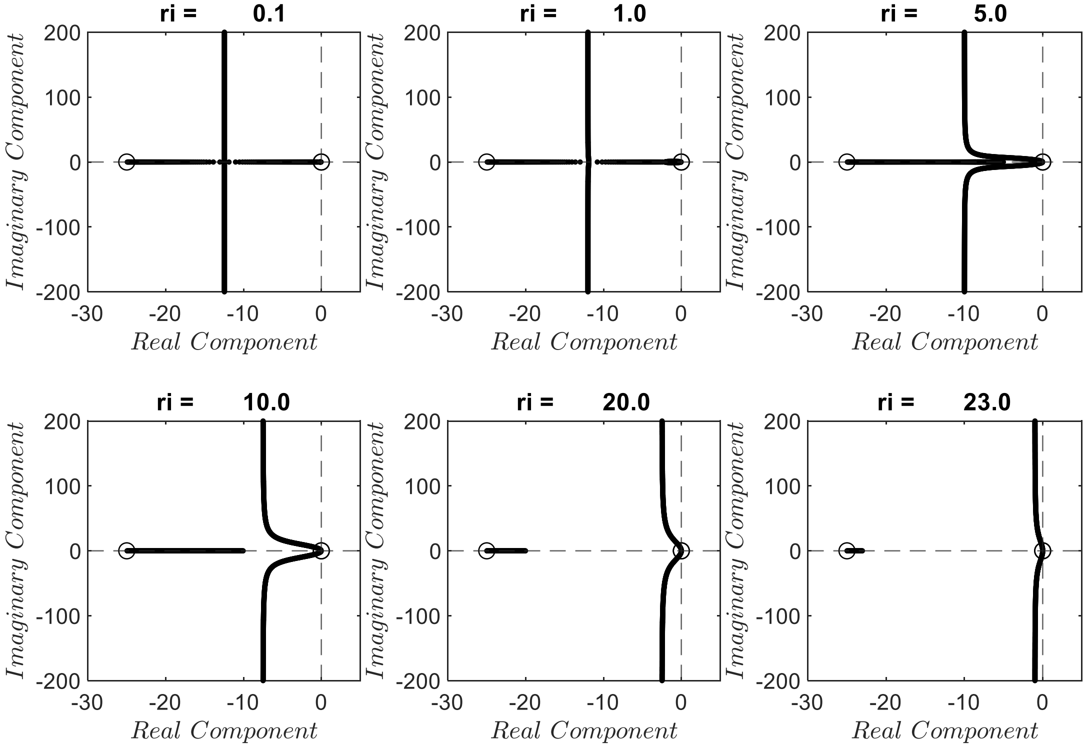

Figure 39. Rotor speed zero root loci of pressure-regulated system with PI-control for chosen values of $r_i \leq 23$

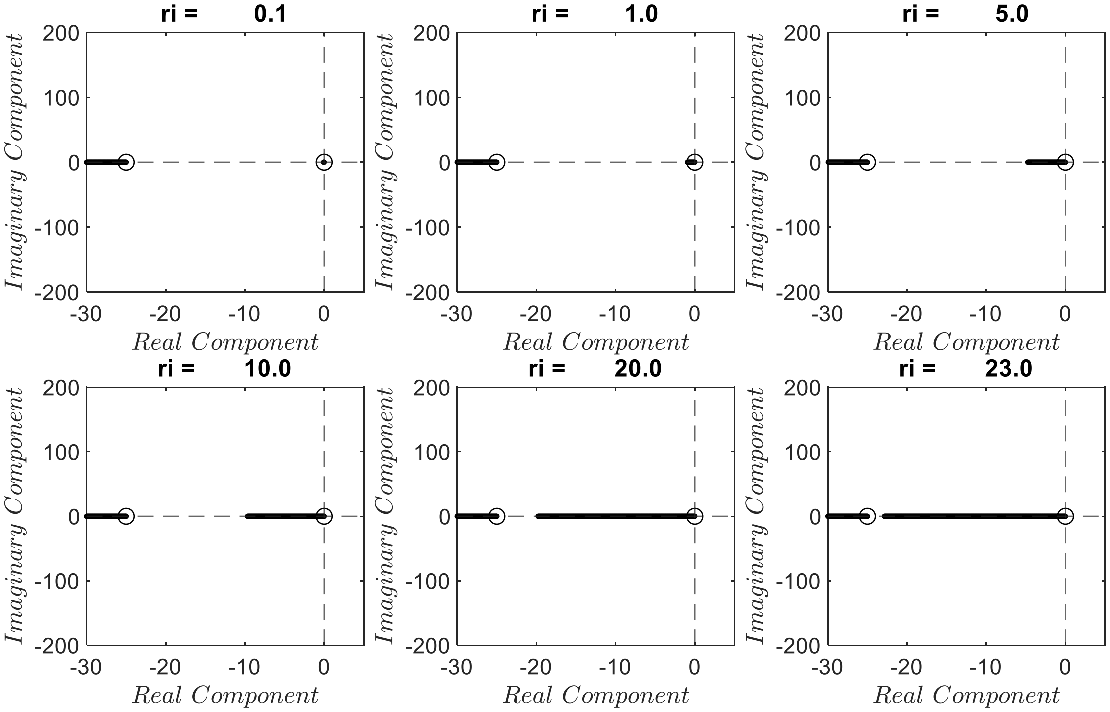

Figure 40. Pressure zero root loci of pressure-regulated system with PI-control for chosen values of r_i

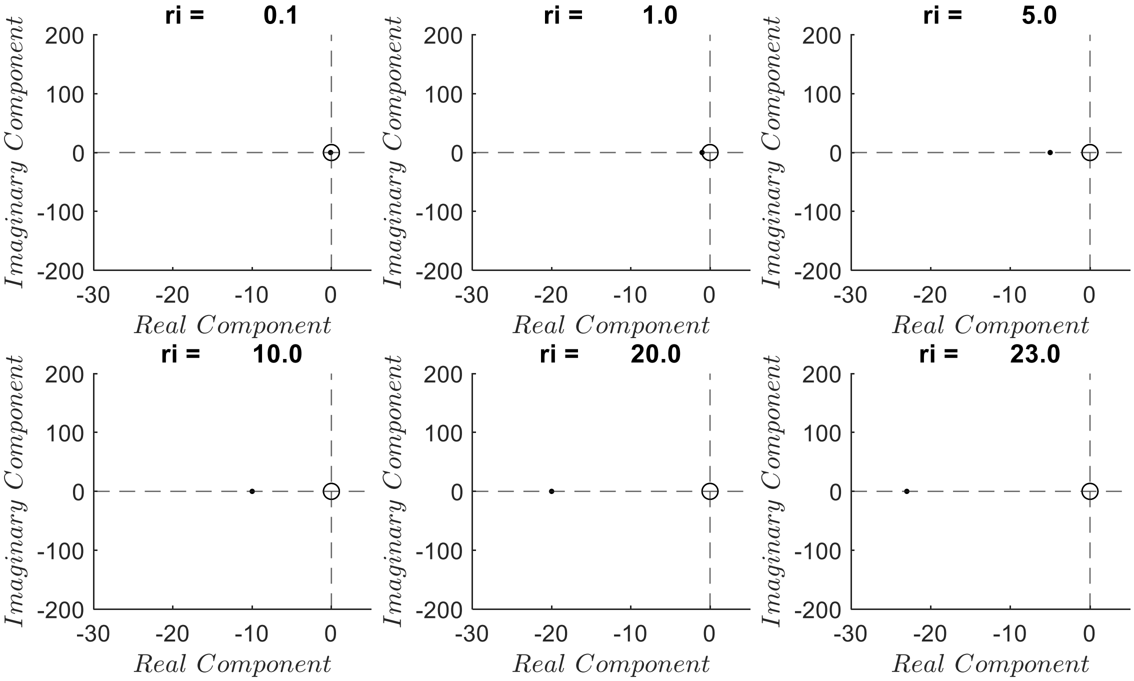

Figure 41. Swashplate zero root loci of pressure-regulated system with PI-control for chosen values of r_i

The closed-loop rotor speed zero branches follow similar but not identical trajectories as the closed-loop pole branches so they will mitigate the effects of the complex poles in the rotor speed response. However, the pressure and swashplate zeros stay on the real axis so the pressure and swashplate responses will still be poorly damped. Regardless of K_p and K_i, the two complex poles have large imaginary components causing poorly damped response.

Appendix 3: Root Loci Tuning for PID-Controlled Systems

The PID-controlled systems here have three control degrees of freedom: K_p, K_i and K_d. $r_i = K_i/K_p$ and $r_d = K_d/K_p$ can be used to shape the loci. Varying r_i and r_d instead of K_i and K_d preserves the loop gain K_p as r_i and r_d vary. Figure 42 shows pole root loci for the pressure-regulate0d system with various chosen values of r_i and r_d.

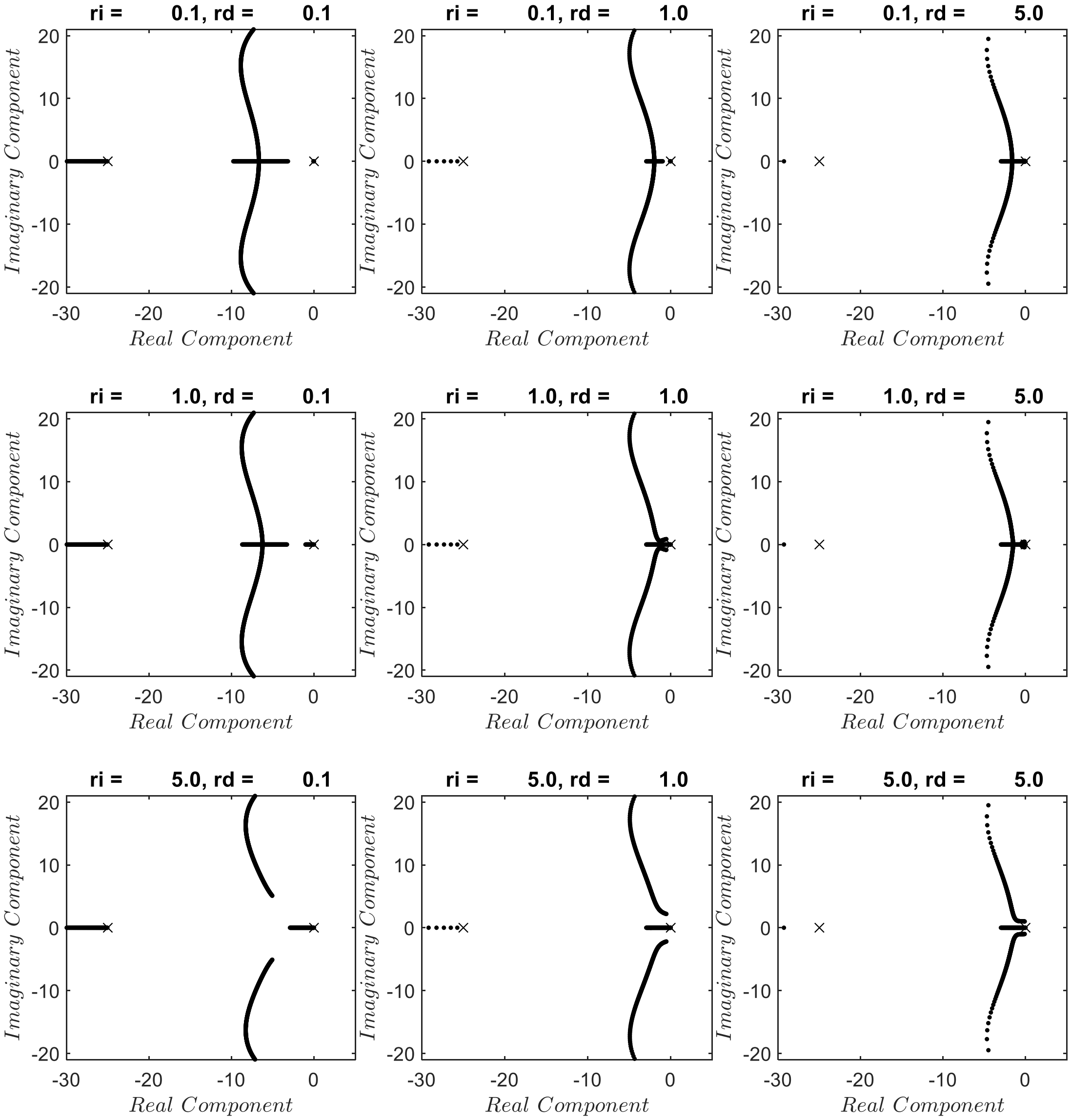

Figure 42. Root loci of pressure-regulated system with PID-control for chosen r_i and r_d

These loci apply for both pressure- and rotor speed-regulated systems because the systems' transfer functions are identical for all r_i and r_d if $K_{p,rs} = 2K_{p,pr}$. This means the branches for the chosen pairs of r_i and r_d are equal but the exact closed-loop pole locations are only equal for $K_{p,rs} = 2K_{p,pr}$. The open-loop poles are comprised of a stable pair of complex conjugates, an integrator and a significantly faster stable pole at $s = -\psi$. Loci located along the real axis much farther from the origin than $s = -3$ are dynamically negligible and will not be discussed. The branch stemming from $s = -\psi$ falls into this category.

The closed-loop complex branches move toward the negative real axis and either converge on the real axis or asymptotically reach final complex locations near the real axis. The complex branches that converge on the real axis diverge along the real axis, one moving away from the origin and one moving toward it. The branch moving toward the origin can continue with one of two possible outcomes. This branch can either asymptotically approach as far as $s = -3$ or collide with the real branch that stems from the origin which causes the two branches to diverge from the real axis as complex conjugates. This divergence forces the branches to arc toward the imaginary axis, causing their closed-loop poles to approach locations near the imaginary axis.

The closed-loop real branch that stems from the origin moves along the real axis away from the origin. This branch can converge with another as previously mentioned. If it does not converge with another branch, it asymptotically approaches a stable position on the real axis. For lower r_i and r_d, neither this branch nor the branch that stems from the fast real open-loop pole moves very much. This slows the system speed of response. For higher r_i and r_d, the complex branches do not converge on the real axis and allow the branch that stems from the origin to reach $s = -3$. This is much less limiting for the system speed of response. r_i and r_d are selected such that the complex conjugates do not converge but stay close to the real axis. As K_p increases, the complex poles tend toward the imaginary axis and the real pole tends toward $s = -3$. So, complex branches that asymptotically approach locations far from the imaginary axis and close to the real axis achieves both design objectives.